The role of Mg(II) in DNA cleavage site recognition in group II intron ribozymes: Solution structure and metal ion binding sites of the RNAmiddle dotDNA complex

Skilandat, Miriam ; Sigel, Roland K O

Abstract: Group II intron ribozymes catalyze the cleavage of (and their reinsertion into) DNA and RNA targets using a Mg^{2+}-dependent reaction. The target is cleaved 3 to the last nucleotide of intron binding site 1 (IBS1), one of three regions that form base pairs with the intron's exon binding sites (EBS1 to -3). We solved the NMR solution structure of the d3 hairpin of the Sc.ai5 intron containing EBS1 in its 11-nucleotide loop in complex with the dIBS1 DNA 7-mer and compare it with the analogous RNA · RNA contact. The EBS1 · dIBS1 helix is slightly flexible and non-symmetric. NMR data reveal two major groove binding sites for divalent metal ions at the EBS1 · dIBS1 helix, and surface plasmon resonance experiments show that low concentrations of Mg^{2+} considerably enhance the affinity of dIBS1 for EBS1. Our results indicate that identification of both RNA and DNA IBS1 targets, presentation of the scissile bond, and stabilization of the structure by metal ions are governed by the overall structure of EBS1 · dIBS1 and the surrounding loop nucleotides but are irrespective of different EBS1 · (d)IBS1 geometries and interstrand affinities.

DOI: https://doi.org/10.1074/jbc.M113.542381

JBC Papers in Press. Published on June 3, 2014 as Manuscript M113.542381
The latest version is at http://www.jbc.org/cgi/doi/10.1074/jbc.M113.542381

The Role of Magnesium(II) for DNA Cleavage Site Recognition in Group II Intron Ribozymes – Solution Structure and Metal Ion Binding Sites of the RNA·DNA Complex.

Miriam Skilandat and Roland K. O. Sigel[1]

From the Department of Chemistry, University of Zurich, Winterthurerstrasse 190, CH-8057 Zurich, Switzerland

Running Title: *EBS1·dIBS1-hybrid structure and metal ion binding*

To whom correspondence should be addressed: Roland K. O. Sigel, Department of Chemistry, University of Zurich, Winterthurerstrasse 190, CH-8057 Zurich, Switzerland
Tel: +41 44 6354652; Fax: +41 44 6356802; Email: roland.sigel@chem.uzh.ch

Keywords: Nucleic acid structure, RNA, DNA, Hybrid, NMR, Ribozyme, Metal ion binding

Background: Group II introns cleave DNA and RNA 3' of a short duplex formed between the intron and the target.
Results: We present the NMR structure of this hybrid duplex and describe two distinct Mg^{2+} binding sites.
Conclusion: The hybrid is asymmetric and strongly stabilized by Mg^{2+} binding.
Significance: Site-bound metal ions are crucially important for group II intron cleavage site recognition.

ABSTRACT

Group II intron ribozymes catalyze the cleavage of (and their reinsertion into) DNA and RNA targets using a Mg^{2+}-dependent reaction. The target is cleaved 3' to the last nucleotide of the intron binding site (IBS)1, one of three regions that form base pairs with the intron's exon binding sites (EBS)1-3. We solved the NMR solution structure of the d3' hairpin of the *Sc*.ai5γ intron containing EBS1 in its 11 nt loop in complex with the dIBS1 DNA 7mer and compare it to the analogous RNA·RNA contact. The EBS1·dIBS1 helix is slightly flexible and non-symmetric. NMR data reveal two major-groove binding sites for divalent metal ions at the EBS1·dIBS1 helix and Surface Plasmon Resonance experiments show that low concentrations of Mg^{2+} considerably enhance the affinity of dIBS1 for EBS1. Our results indicate that identification of both RNA and DNA IBS1 targets, presentation of the scissile bond, and stabilization of the structure by metal ions are governed by the overall structure of EBS1·dIBS1 and the surrounding loop nucleotides but are irrespective of different EBS1·(d)IBS1 geometries and interstrand affinities.

INTRODUCTION

Group II introns are large ribozymes and mobile genetic elements capable of catalyzing their own splicing reaction (1-3). During splicing, the intron RNA excises itself from an RNA transcript in two sequential phosphotransesterification reactions that yield the two ligated exons and the excised intron in a lariat structure. Both steps of splicing are reversible, which enables the intron to reinsert into intronless sites on RNA or DNA, a process which is referred to as reverse splicing or retrohoming, if genomic DNA is the target of reinsertion (4-8). The most extensively studied example of the retrohoming pathway is the *L. Lactis Ll*.LtrB group IIA intron and requires an intron-encoded protein (IEP) (9,10) encoded in an open reading frame in domain 4 of the intron. During retrohoming, the IEP unwinds the DNA locally to allow hybridization of the spliced lariat intron RNA and the target DNA. The intron catalyzes the reverse splicing by cleaving the target strand and ligating its own termini to the flanking DNA. The opposite strand is cleaved by the IEP endonuclease domain and the reverse transcriptase domain of the IEP transcribes the complementary cDNA from the intron RNA template. The removal of the RNA and the synthesis and ligation of the DNA, which replaces

it, are catalyzed by host proteins and complete the insertion process. As mobile genetic elements, group II introns resemble non-LTR-retrotransposons (11) and they perform splicing in a very similar way as the eukaryotic spliceosome does (12,13). These parallels gave rise to the idea that group II introns might be ancestors of both the spliceosome and non-LTR-retroelements suggesting pivotal evolutionary importance of group II introns for the shaping of eukaryotic genomes (14,15).

In both splicing and reverse splicing, exon-intron recognition is mediated by base pair formation between the exon binding sites (EBS) of the intron and the corresponding intron binding sites (IBS) on the exons (16). In the case of group IIB introns, there are three such contacts. EBS1 – with 5-7 nt the longest of the three sequences – and EBS2 bind the 5'-exon (17) while EBS3 forms a single base pair with the 3'-exon (Figure 1A and 1C). Additionally, another base pair within the intron, the so-called δ-δ' interaction helps to stabilize the intron-exon contacts by positioning the sequentially distant EBS1 and EBS3 close to each other (Figure 1C) (18,19). The EBS1·IBS1 interaction confers high specificity to the site of reinsertion of the intron, thus preventing insertion into sites from which the intron cannot splice again. However, it has been shown that EBS sequences are not conserved within different group II introns (17,20,21). For this reason, any desired sequence can be bound and cleaved by the intron in *trans* as long as the EBS and IBS sequences are complementary (22-25). This characteristic endows group II introns with a remarkable potential for gene therapy applications (26).

Group II introns consist of 6 domains (DI-DVI) radiating from a central wheel (Figure 1A). DI, containing the EBS sequences, is the largest and constitutes an autonomous folding entity to which other domains dock in the folding process (27-29). Together with DV it forms the minimal structure required for catalytic activity of the intron (30,31). Mg^{2+} ions play a critical role for both structure and function of group II introns and large ribozymes in general (32-35). Formation of a stable tertiary structure of the group II intron is dependent on the presence of divalent metal ions (28,36,37). Moreover, several metal ion binding sites have been located in the active site (38-40) and a two-metal ion mechanism (41,42) has been suggested to underlie intron catalysis (43,44). In-cell studies establishing a correlation between the intracellular Mg^{2+} concentration and the frequency of splicing and retrohoming buttress the relevance of Mg^{2+} for group II intron catalysis (45-48). The importance of the identity of the divalent metal ions bound to the intron is underscored by the finding that the presence of Mn^{2+} can lead to a shift of the cleavage site (49) and that already low amounts of Ca^{2+} decrease the turnover rate by 50 % in the *Sc*.ai5γ intron (50).

Although a wealth of genetic and biochemical investigations have shed light on group II intron function, the information on tertiary structure is sparse. The group IIC intron of *Oceanobacillus iheyensis* is the only entire group II intron for which crystal structures are published (44,51-54).

In this paper, we present the first structure of the complex between the d3'EBS1 hairpin and the dIBS1 DNA using EBS1·dIBS1 of the intron *Sc*.ai5γ, found in mitochondrial transcripts of *S. cerevisiae*, as a model construct. We focus on a detailed analysis of the metal ion binding properties of the complex as determined by NMR spectroscopy and Surface Plasmon Resonance (SPR). As the same catalytic mechanism underlies intron-catalyzed DNA and RNA cleavage, we compare our data to the structure and metal ion binding of the analogous d3'EBS1·IBS1 homoduplex construct (55) and discuss common features relevant for stable binding of the target and for the recognition of the cleavage site.

EXPERIMENTAL PROCEDURES

NMR sample preparation – In d3'EBS1·dIBS1 (Figure 1B), nucleotides 5-25 of the hairpin correspond to the sequence of the d3' hairpin from domain I of the *Sc*.ai5γ group II intron (Figure 1A and 1B) except for nucleotides 15 and 17 in EBS1 that are adenines in the wild type sequence. In order to have a suitable starting sequence for *in vitro* transcription (56) and a more stable hairpin stem, four base pairs were added to the stem (box in Figure 1B). The dIBS1 sequence is a deoxyribonucleotide 7mer corresponding to the wild type sequence of dIBS1 except for T-to-G mutations in position 61 and 63 matching the mutations of EBS1. The resulting GC base pairs are required to achieve a stable enough duplex formation for NMR investigation (Table 4, see also references (55,57)). RNA was transcribed *in*

vitro according to standard procedures (58) with T7 RNA polymerase produced in our lab. Isotope-labeled RNA was obtained by transcribing with uniformly ^{15}N,^{13}C labeled NTPs (Silantes GmbH, Germany) or with selectively deuterated NTPs (Cambridge Isotope Laboratories Ltd., USA). The RNA was purified by polyacrylamide gel electrophoresis using acrylamide/bisacryamide concentrations of 15-18 % and recovered from the gel by electroelution (Elutrap Electroelution System, Whatman, UK), annealed by dissolving it in an excess of water at 85 °C and rapidly cooling in icy water after 2 min of incubation. RNA was washed with 1 M KCl, pH 8 and H_2O and concentrated by ultrafiltration in Vivaspin® devices (Sartorius Stedim Biotech S.A., Germany). The dIBS1 deoxyribonucleotide 7mer was purchased HPLC-purified from Microsynth (Balgach, Switzerland) and desalted by gelfiltration on illustra™ NAP-10 columns (GE Healthcare, UK). The concentration of d3'EBS1 and dIBS1 was determined by UV/VIS-spectroscopy using extinction coefficients ε_{260} of 303.3 $mM^{-1}cm^{-1}$ for d3'EBS1 and of 63.9 $mM^{-1}cm^{-1}$ for dIBS1. dIBS1 was added to d3'EBS1 to an excess of 10 % to avoid the presence of unbound d3'EBS1. All samples contained between 0.5 and 0.8 mM of d3'EBS1·dIBS1 as well as 110 mM KCl and 10 µM EDTA. Prior to the acquisition of NMR data, each sample was lyophilized and dissolved in 100 % D_2O (Armar Chemicals, Switzerland) or 90 % H_2O/ 10 % D_2O and the pH was adjusted to 6.4 in D_2O, corresponding to a pD of 6.8 (59), or to a pH of 6.8 in 90 % H_2O/ 10 % D_2O.

NMR spectroscopy − All spectra were recorded on a Bruker Avance 500 MHz spectrometer with a 5 mm CRYO QNP probehead with z-gradient coil, a Bruker Avance 600 MHz spectrometer with a 5 mm CRYO TCI inverse triple-resonance probehead with z-gradient coil or on a Bruker Avance 700 MHz spectrometer with a 5 mm CRYO TXI inverse triple-resonance probehead with z-gradient coil. Non-exchangeable proton resonances were assigned using [^1H,^1H]-NOESY spectra with a mixing time of 250 ms, 180 ms or 60 ms at a temperature of 20 °C, 25 °C or 30 °C. Assignment of H2' proton resonances was validated by [^1H,^1H]-NOESY spectra of partially deuterated RNA. [^1H,^1H]-TOCSY spectra with 45 ms mixing time were recorded to assess sugar puckers. The signal of residual water was suppressed with presaturation pulses. *F1,F2*-[^{13}C,^{15}N]-filtered [^1H,^1H]-NOESY and [^1H,^1H]-TOCSY spectra (60) with WATERGATE pulse sequences for water suppression were recorded of ^{13}C, ^{15}N-labeled d3'EBS1 with natural abundance dIBS1 to validate the assignment of dIBS1 resonances. Exchangeable protons were assigned using [^1H,^1H]-NOESY spectra with a WATERGATE pulse sequence for water suppression in 90 % H_2O/ 10 % D_2O at 5 °C and 20 °C. ^{13}C resonances were attributed in [^1H,^{13}C]-HSCQ spectra and ^{15}N resonances were attributed using SOFAST [^1H,^{15}N]-HMQC spectra in 90 % H_2O/ 10 % D_2O at 5 °C, 20 °C and 25 °C. All proton resonances are directly referred, and ^{13}C and ^{15}N resonances are indirectly referred to DSS proton resonances (61). All processing was done in TopSpin 3.0, assignments were carried out with the program Sparky (http://www.cgl.ucsf.edu/home/sparky/). Residual Dipolar Couplings (RDCs) were determined by recording a series of *J*-modulated [^1H,^{13}C]-HSCQ spectra (62) that were recorded in the presence and in the absence of ~17 mg/mL filamentous Pf1 bacteriophages (ASLA Biotech Ltd., Latvia) used for alignment. Peak volumes were determined using the program CCPNmr Analysis (63) and fitted in with the program gnuplot (http://www.gnuplot.info/).

Mg^{2+}-, Mn^{2+}- and hexamminecobalt(III) titrations − For Mg^{2+} titrations, a d3'EBS1·dIBS1 sample in 100 % D_2O was titrated with increasing amounts of $MgCl_2$ (0, 0.5, 1, 1.5, 2, 3, 4, 5, 6, 8, and 10 mM) and a [^1H,^1H]-NOESY spectrum (25 °C) was recorded at each step. All spectra were assigned and chemical shifts were analyzed by creating bar plots in gnuplot (http://www.gnuplot.info). A d3'EBS1·dIBS1 sample in 100 % D_2O was titrated with increasing amounts of $MnCl_2$ (0, 25, 50, 75, 100, 150 and 200 µM) recording a [^1H,^1H]-NOESY at 25 °C for each step. Additionally, a partially deuterated sample was titrated with 0, 20, 40, 60, 80, 100 µM $MnCl_2$ in the same way. Line broadening was assessed visually using the program Sparky (http://www.cgl.ucsf.edu/home/sparky/). Chemical shift changes caused by $[Co(NH_3)_6]^{3+}$ were determined in the same way as described above for Mg^{2+}, titrating a sample in 100 % D_2O with 0, 0.5, 0.75, 1.25 and 2 mM $[Co(NH_3)_6]Cl_3$.

Structure calculations & analysis − Estimates

of interproton distances were obtained from [^{1}H,^{1}H]-NOESY data. Peak volumes were integrated using Sparky (http://www.cgl.ucsf.edu/home/sparky/); the distance was calibrated to the fixed H1'-H2' distance (2.8-3.0 Å) and H5-H6 distance (2.4 Å) of pyrimidines using DYANA (64). According to this, all assigned cross peaks were classified as strong (1.8-3.0 Å), intermediate (1.8-4.5 Å), weak (3-6 Å) or very weak (4-7 Å).

Sugar pucker torsional angle restraints were set according to the intensity of the intraresidue H1'-H2' cross peaks in [^{1}H,^{1}H]-TOCSY spectra. Residues with strong cross peaks (A10, U11, U12) were confined to south (C2'-*endo*) conformation (δ = 145° ± 30°, $\nu1$ = 25°, $\nu2$ = –35°, ± 15°), residues with absent cross peaks were restrained to north (or C3'-*endo,* δ = 85°, $\nu1$ = –25°, $\nu2$ = 37°, ± 30°). For residues with intermediate cross peaks (G1, C29) no sugar pucker restraints were set. For the RNA residues in helical regions, with C3'-*endo* sugar puckers and typical alternating NOESY cross peak intensity pattern, the backbone torsion angles α, β, γ, ε, and ζ were set to the values of classical A-form helix (α = –62°, β = –180°, γ = 47°, ε = –152°, ζ = –74, ± 10°). χ angles were set to –160 ± 20° (RNA) and –120 ± 40° (DNA) according to the intensity of the intra-residue H1'-H8/6 cross peaks in the [^{1}H,^{1}H]-NOESY with 60 ms mixing time. Due to the absence of down-field shifted ^{31}P resonances, α and ζ dihedral angles of all RNA and DNA residues not restrained to A-form geometry were set to 0° ± 120° to exclude the *trans* range (65). For dIBS1 residues, the spectral data did not allow for a clear decision on the sugar conformation or backbone geometry (see Results section for details). We hence refrained from restraining both sugar pucker defining angles and backbone torsional angles other than α and ζ to any specific ranges.

Base pair formation was validated by the presence of characteristic interstrand [^{1}H,^{1}H]-NOESY cross peaks. In calculations, hydrogen bonds within base pairs were maintained by applying distance restraints between donor hydrogen and acceptor and between donor and acceptor atoms and by enforcing planarity.

From the extended RNA and DNA chain, 200 starting structures were calculated by restrained molecular dynamics (rMD) with CNS version 1.21. (66,67) applying all but RDC restraints. A high temperature stage of 40 ps at 20000 K was followed by two cooling stages of 90 ps in torsional space and 30 ps in cartesian space. The 20 structures of lowest energy were subjected to a refinement by 88 ps of rMD cooling from 3000 K to 50 K. For this step, XplorNIH version 2.3 (68,69) was used and 21 ^{1}H-^{13}C RDCs were included. The axial and rhombic component of the alignment tensor were estimated using PALES (70) and determined by an extensive grid search (71) to be −27.3/0.08. Throughout the refinement, the force constant for RDCs was gradually increased from 0.01 kcal mol^{-1}Hz^{-2} to 1 kcal mol^{-1}Hz^{-2}. In the resulting 200 refined structures, some of the structures contained one or two NOE violations from the 19th conformer on. Accordingly, only the 18 conformers of lowest energy which satisfied all given restraints were subjected to further analysis. The structure ensembles were analyzed using MOLMOL (72), the electrostatic surface potential was determined with the PDBPQR v1.8 webserver (73,74), http://nbcr-222.ucsd.edu/pdb2pqr_1.8/) and visualized with APBSTools2 v1.4.1 in Pymol. Analysis of sugar and backbone geometry was performed with the webservers web3DNA (75,76) and PROSIT (http://cactus.nci.nih.gov/prosit/).

Calculation of the d3'EBS1·dIBS1 structure with bound [Co(NH$_3$)$_6$]$^{3+}$ ions − In order to localize binding sites for [Co(NH$_3$)$_6$]$^{3+}$ ions in d3'EBS1·dIBS1, [^{1}H,^{1}H]-NOESY spectra of d3'EBS1·dIBS1 were recorded in the presence of 1 mM [Co(NH$_3$)$_6$]$^{3+}$ (for the non-exchangeable protons, 25 °C) and 1.5 mM [Co(NH$_3$)$_6$]$^{3+}$ (exchangeable protons, 5 °C). Cross peaks between RNA or DNA protons and [Co(NH$_3$)$_6$]$^{3+}$ protons were assigned in Sparky. All nucleic acid protons displaying such cross peaks to the ammine protons were clustered according to their position in the solution structure calculated in the absence of [Co(NH$_3$)$_6$]$^{3+}$ (Table 1). For rMD calculations of the structures with bound [Co(NH$_3$)$_6$]$^{3+}$, a loose distance restraint of 3-7 Å between the Co^{3+} central ion and each nucleic acid proton displaying an NOE cross peak to the ammine protons was added in the refinement. As all ammine protons of [Co(NH$_3$)$_6$]$^{3+}$ resonate at one common frequency and therefore cannot be distinguished, the distance to the Co^{3+} central ion was used for the restraints (77). In the resulting ensemble, the 6 out of 10 lowest energy conformers that had no violations of NOE or dihedral angle restraints were used for further analysis.

SPR sample preparation and measurements − All data were recorded on a Biacore T100 system. d3'EBS1/d3'EBS1wt coupled to biotin via a four-uracil 3'-overhang were purchased PAGE-purified from IBA GmbH (Göttingen, Germany) and used as ligands. (d3'EBS1/d3'EBS1wt)-4U-biotin was immobilized on a Series S Sensor Chip SA (GE Healthcare, UK) pre-coated with Streptavidin on a carboxymethyldextran surface or on a carboxymethyldextran hydrogel chip (XanTec bioanalytics, Düsseldorf, Germany), coated with neutravidin in our lab. The surface was pre-treated with 3-5 injections of 1 M NaCl, 50 mM NaOH lasting 50 s at a flow of 30 µL/min. Immobilization was carried out by injecting 200 µg/mL d3'EBS1-4U-biotin for 10 min at a flow of 5 µL/min. All experiments were performed in 10 mM MOPS, 107 mM KCl (I = 110 mM), 0.05 % Polysorbate 20, pH 6.8. The dIBS1 and dIBS1wt DNA and IBS1 and IBS1wt RNA 7mers were used as analytes for kinetics measurements. dIBS1 and dIBS1wt were acquired and treated as described for NMR experiments in the article. IBS1 and IBS1wt were purchased double-HPLC purified from IBA GmbH (Göttingen, Germany). Each kinetics run was preceded by five startup cycles injecting the current running buffer. The system was normalized using BIA normalizing solution (GE Healthcare, UK). The flow rate was 30 µL/min. In each cycle, the adsorption and desorption was allowed to proceed for 60 s, each followed by 180 s of stabilization. At the end of each cycle, water was injected for 60 s to remove any residual analyte and Mg^{2+} bound to the surface. For all experiments, buffer injections were used for blank subtraction and one or more non-zero concentrations of the analyte were injected twice before and after the highest concentration to monitor that the performance of the surface did not significantly change within one experiment. All analyte samples were injected both into a flow cell where d3'EBS1 was immobilized and in a ligand-free reference flow cell for control and background subtraction. Measurements were repeated on a different sensor chip for confirmation. In order to compare the affinity of dIBS1 and IBS1 to d3'EBS1, kinetics experiments were recorded at 25 °C. Magnesium(II) titrations of dIBS1 and IBS1 binding to d3'EBS1 and dIBS1wt and IBS1wt binding to d3'EBS1wt were performed at 15 °C or 25 °C by adding 0, 1, 2, 5 or 20 mM $MgCl_2$ or 1 mM $[Co(NH_3)_6]Cl_3$ to the running buffer and to the analyte stock. For each concentration of $MgCl_2$ a separate experiment was run. In all experiments, 5-7 non-zero concentrations of the analyte were injected being in the range of 0.25-16 µM for dIBS1, 0.5-45 µM for dIBS1wt, 0.0156-8 µM for IBS1 and 0.19-45 µM for IBS1wt. In order to obtain k_{on}, k_{off} and K_D data were fitted and analyzed with the corresponding Biacore T100 evaluation software assuming a 1:1 binding model.

RESULTS

Characterization of dIBS1 binding to EBS1 by NMR spectroscopy − To verify stable formation of the EBS1·dIBS1 hybrid, we used [^{1}H,^{1}H]-NOESY spectra recorded in H_2O (Figure 2A). When d3'EBS1 or dIBS1 are measured separately in solution, the imino protons of the recognition sequences (G13, G14, U18 and G19 of EBS1 and of G61, T62, G63 and T64 of dIBS1) cannot be observed as these regions are largely unstructured and the protons exchange rapidly with the solvent. The presence of resonances for each of these protons (colored labels in Figure 2A) and of cross peaks within and between EBS1 and dIBS1 is a clear indication that EBS1 and dIBS1 are indeed fully base paired. Each imino proton in the d3' stem can be attributed to one resonance (black labels in Figure 2A), their chemical shifts being very similar to the ones observed for the unbound d3'EBS1 (55) proving that addition of dIBS1 does not interfere with the base pairing in the stem.

Sequence-specific assignment of the resonances of the non-exchangeable d3'EBS1 and dIBS1 protons was accomplished using standard [^{1}H,^{1}H]-NOESY spectra and *F1,F2*-[^{13}C,^{15}N]-filtered NOESY spectra (60) (Figure 2B). The chemical shifts of protons from the RNA stem are in excellent accordance with previously published ones for unbound d3'EBS1 (55). The sequential cross peaks between U12 in the loop and G13 and G14 in EBS1 are very low in intensity (data not shown), probably due to an unusual geometry at residue G13. The remaining loop residues display typical spectral features of an A-form RNA except for A10-U12 whose ribose moieties are in C2'-*endo* conformation according to the [^{1}H,^{1}H]-TOCSY data (3B, see also Experimental section).

For dIBS1, the cross peak intensity pattern in the [^{1}H,^{1}H]-NOESY and [^{1}H,^{1}H]-TOCSY (Figure

3 and Figure 4) reveals an unusual geometry of the DNA strand. In the [^{1}H,^{1}H]-TOCSY all dIBS1 nucleotides, except for C65 that displays the C3'-*endo* cross peak pattern, display cross peaks of intermediate intensity for both the H1'-H2' correlation and the H3'-H4' correlation, which is untypical for a pure C3'-*endo* or C2'-*endo* conformation. This can signify either conformational flexibility of the deoxyribose rings or a rare O4'-*endo* conformation. The latter however is associated with a very short H1'-H4' distance (2 Å) (55), which the NOESY data only suggest for T62 and T64 (data not shown). Additionally, the intensity difference between the H2'-H6/8 and the H2''-H6/H8 NOESY cross peaks (Figure 3) and a systematically higher $J_{1'2'}$ than $J_{1'2''}$ coupling characteristic for B-form DNA are not observed. It is thus clear that the DNA neither adopts the A-form of its EBS1 binding partner nor B-form geometry which is the preferred one of DNA. Additionally, the rather broad DNA cross peaks suggest conformational exchange within dIBS1 (Figure 3).

The solution structure − The ensemble of the 18 d3'EBS1·dIBS1 conformers (Figure 5A) of lowest energy shows good convergence of the heavy atoms, represented by the low overall root mean square deviation (RMSD) of 1.00 Å (Table 2). In the short helix formed by dIBS1 and EBS1 (Figure 5B), the backbone trajectory of the dIBS1 strand varies. The stem, which is a regular A-form helix and the EBS1·dIBS1 helix are nearly parallel to each other but slightly shifted in all 18 conformers. This shift is due to the uneven number of unpaired bases on the 5'- and 3'-side of EBS1 (see A10, U11, U12 and A20 in Figure 5D). A20 on the 3'-end of the loop forms a bridge between the stem and the EBS1·dIBS1 helix by stacking in between their terminal base pairs C59·G19 and U9·G21. Opposite of A20, A10 on the 5'-end of the loop is stacked on U9 and in some conformers U11 and U12 also display stacking interactions (Figure 5D). In this arrangement, it is probable that hydrogen bond formation between A10N61 and A20N1 further stabilizes the structure. The single-stranded nucleotides not only stabilize the junction between the d3' stem and EBS1·dIBS1 but also seem to fix the position of the 5'-end of dIBS1. The observation of several cross peaks between protons of C59, the 5' terminal nucleotide of dIBS1 and A10, U11, U12 and A20 (Figure 2B) agree well with the position of C59, which is placed in between A10 and U11 or U12 at the 5'-end of the loop and A20 on the 3'-end (Figure 5D).

In contrast to C59, C65, where cleavage occurs, is in an exposed position. Between U12 and G13 of EBS1, a sharp turn or kink changes the direction of the RNA backbone (Figure 5C). This kink moves the bases of G13 and U12 far apart so that stacking interactions are only possible between G13 and G14. This explains why NOE correlations between U12H1' and G13H8 are extremely weak if observed at all as both protons are separated by a distance greater than 6 Å.

The variable non-standard conformations of EBS1·dIBS1 cause its low stability. − As it was evident from TOCSY and NOESY spectra that dIBS1 does not assume any standard helical conformation and seems to be subject to conformational exchange, we evaluated more closely the geometry of EBS1 and dIBS1 in the hybrid duplex in five of the 18 lowest energy structures with visibly different backbone trajectories on the side of dIBS1 (Figure 5B), representing possible fits to the NOE data. Importantly, no dihedral angle restraints limiting the sugar pucker of the dIBS1 nucleotides were included in the calculation (see Experimental Section). As RNA is conformationally less tolerant than DNA, the geometries of hybrid duplexes are usually reported to be more similar to A-form (78-80). In agreement with this, the EBS1 strand adopts an A-form geometry even in control calculations, where only the α and ζ backbone angles are loosely restrained to the *trans* range, which is in line with the [^{1}H,^{1}H]-NOESY and [^{1}H,^{1}H]-TOCSY data. However, in contrast to EBS1, comparison of the backbone and sugar pucker defining angles (Table 3) of dIBS1 to the standard angles found in A-form or B-form DNA proves that dIBS1 conforms to neither conformation in any analyzed trajectory. Another remarkable feature of the dIBS1·EBS1 duplex is the fact that all of the five conformers have a significantly narrower minor groove than major groove (14.8 Å vs. 16.4 Å, on average) which is normally a feature of B-DNA. The deoxyribose rings of the different dIBS1 nucleotides have different sugar puckers and seem to be able to exchange between similar sugar puckers with the exception of T62 and G63 (O4'-*endo*) and C65 (C3'-e*ndo*) that have the same conformation in all

analyzed structures (Table 3). This asymmetric structure of the EBS1·dIBS1 duplex adds a new variation to the continuum of helical conformations that can be observed for RNA·DNA helices depending on the exact sequence and the distribution of purines and pyrimidines in each strand (81-83).

SPR experiments were performed to investigate the impact of the conformational heterogeneity on EBS1·dIBS1 stability. At 25 °C, in the absence of any divalent metal ions, the K_D of EBS1·dIBS1 is 29 ± 6 μM (Table 4). This value is at the upper limit of what can be accurately measured by the instrument and hence should be considered an estimate. For comparison, the K_D of the RNA·RNA duplex of EBS1·IBS1 is about 200 times lower (Table 4), owing to the much lower dissociation rate of IBS1 RNA from EBS1. Given that the EBS1·IBS1 homoduplex is a regular A-form helix (55), the heterogenous geometry of the EBS1·dIBS1 hybrid must be causing this drastically decreased affinity. To get more reliable data for the EBS1·dIBS1 interaction, we repeated the experiments at 15 °C where the affinity is higher and determined a K_D of 1.65 ± 0.2 μM (Table 4). We also tested the influence of low millimolar concentrations of Mg^{2+} on the stability of the interaction (Figure 6 and Table 4). Strikingly, in the presence of only 1 mM Mg^{2+}, which is in the range of the physiological intramitochondrial Mg^{2+} concentration (84,85), k_{off} and, consequently K_D decrease by a factor of 6 and 4.6, respectively, and in the presence of 2 mM Mg^{2+} the K_D is about one order of magnitude lower than in the absence of Mg^{2+}. This demonstrates that, Mg^{2+} is of vital importance to stabilize EBS1·dIBS1 by inhibiting dissociation of the two strands. Importantly, all experiments were carried out in a buffer with an equal ionic strength of 110 mM KCl sufficient to provide charge screening of the polyanionic sugar-phosphate backbone. Consequently, the stabilization induced by Mg^{2+} is of a specific nature and not simply a charge-compensation effect. Also the affinity of the RNA·RNA contact is increasing upon addition of Mg^{2+} (Table 4). While the RNA·RNA contact shows very similar K_D in 1 and 5 mM Mg^{2+}, suggesting that the maximum affinity has been reached, the K_D of the RNA·DNA contact seems to stabilize only at 10-20 mM Mg^{2+}. Also $[Co(NH_3)_6]^{3+}$ enhances the affinity of dIBS1 for d3'EBS1. $[Co(NH_3)_6]^{3+}$ is a kinetically stable complex, which mimics a hexahydrated Mg^{2+} ion. It thus probes for outersphere binding events of Mg^{2+}, that means a coordination mediated by the water ligands (86). In 1 mM $[Co(NH_3)_6]^{3+}$, the K_D of EBS1·dIBS1 is 0.05 μM (k_{on}=0.14 $\mu M^{-1}s^{-1}$, k_{off}=0.008 s^{-1}, 15 °C) and thus comparable to the values obtained in 20 mM Mg^{2+} (Table 4). $[Co(NH_3)_6]^{3+}$ binds to nucleic acids with higher affinity than Mg^{2+} (87,88), explaining the stronger stabilization effect. The ability of $[Co(NH_3)_6]^{3+}$ to stabilize EBS1·dIBS1 suggests that specific innersphere contacts between Mg^{2+} and EBS1·dIBS1 are not required for the stabilization.

For comparison, SPR data for the wild type sequences of d3'EBS1 and (d)IBS1 were collected. The wild type EBS1(d)IBS1 helix has two A·U base pairs (instead of C·G) in positions 15·63 and 17·61 (Figure 1B, see Experimental Section) which is reflected in the drastically lower stabilities of wild type d3'EBS1·(d)IBS1 (Table 4). Just like the mutant, the wild-type contact is efficiently stabilized by Mg^{2+}-addition. In fact, precise rate constants can only be measured in the presence of at least 5 mM Mg^{2+}.

Two metal ion binding sites are located in the EBS1·IBS1 region. − As Mg^{2+} is critical not only for EBS1·dIBS1 stability but for the folding of group II introns and retrohoming in general, we localized Mg^{2+} binding sites by a combination of Mg^{2+}, Mn^{2+} and $[Co(NH_3)_6]^{3+}$ titrations.

To determine Mg^{2+} binding sites, an NMR sample was titrated with millimolar concentrations of Mg^{2+} and $[Co(NH_3)_6]^{3+}$. A plot of the chemical shift differences Δδ of the protons of d3'EBS1·dIBS1 in the presence of 3 mM Mg^{2+} and 2 mM $[Co(NH_3)_6]^{3+}$ is depicted in Figure 7. In the middle of the d3' stem the protons of the two base pairs G4·C26 and U5·A25 react to Mg^{2+} addition with intermediate chemical shift changes (Figure 7A). U5H6 and G4H8 resonances also shift strongly in the presence of the larger $[Co(NH_3)_6]^{3+}$ molecule indicating that the d3' stem contains a binding site that is accessible for both hydrated and bare Mg^{2+} ions.

In the loop region (Figure 7B), U11H1', U12H1' and A20H8 and H2 display intermediate Δδ values while A10H2, G21H1' and C59H6 experience strong chemical shift changes > 0.05 ppm in the presence of both Mg^{2+} and $[Co(NH_3)_6]^{3+}$. C59H6 is most affected, moving by

0.074 ppm. These findings suggest that the U9·G21 wobble pair that closes the loop, the adjacent single stranded region and C59 constitute a Mg^{2+} binding site. In a similar titration experiment of [^{1}H,^{15}N]-HSQC correlations (data not shown), the chemical shifts of A10N3 and A20N1 changed by 0.5 ppm upon addition of 3.5 mM Mg^{2+} which corroborates this finding. G13 proton cross peaks were not observable during the titration with Mg^{2+} but addition of 2 mM $[Co(NH_3)_6]^{3+}$ has a large impact on G13H8. Also the H1' of G13 and H5 of C65 experience intermediate Δδ in reaction to both $[Co(NH_3)_6]^{3+}$ and Mg^{2+}. This indicates a second binding site near the other end of the EBS1·dIBS1 helix. Within the EBS1·dIBS1 interaction, the A60·U18 base pair is most influenced by Mg^{2+}. H1' and H8 of G1 display very drastic shifts in the presence of Mg^{2+}, that result from Mg^{2+} binding to the di- or triphosphate moiety only present on the 5' nucleotide (39,89). As this binding site, which also causes the Δδ of C29 and G2 protons, does not exist in the context of the whole intron, we will not discuss it any further.

A Mg^{2+}-induced chemical shift change of a proton can be the result of coordination of Mg^{2+} at the same residue or of subtle structural rearrangements caused by Mg^{2+} coordination in the vicinity. It can also be a mixture of both effects. However, the relative cross peak intensities in fingerprint regions such as the H1'-H6/8 and H2'/H2''-H6/8 cross peaks in the [^{1}H,^{1}H]-NOESY and the intense A10-U12 H1'-H2' C65 H3'-H4' cross peaks in the [^{1}H,^{1}H]-TOCSY (see above) remain unchanged in the presence of up to 4 mM Mg^{2+} and 2 mM $[Co(NH_3)_6]^{3+}$ (data not shown)[2]. This means that neither metal ion causes significant changes in the d3'EBS1·dIBS1 structure.

To locate Mg^{2+} binding sites more precisely, titration experiments were conducted with metal ions that affect NMR parameters other than the chemical shift. Mn^{2+} is a paramagnetic metal ion. Its binding to RNA at specific sites promotes relaxation of the protons in the vicinity depending on the distance between the manganese and the proton nucleus (90). At low ratios of Mn^{2+} to RNA (1:100), selective broadening of the resonances in Mn^{2+} binding sites can be monitored (91,92) undisturbed by structural rearrangements. We therefore recorded [^{1}H,^{1}H]-NOESY spectra in the presence of different micromolar Mn^{2+} concentrations (Figure 8). At 60 μM, very few peaks are already broadened below the detection limit thereby indicating good binding sites for Mn^{2+}. Among the central residues in the d3' stem only G4 and A3 appear to be sensitive to the presence of Mn^{2+}. In the loop region, various protons are influenced by Mn^{2+}, but less strongly. The cross peaks between A10 and U11 and between U11 and U12 are not observable anymore in 60 μM Mn^{2+}. A20H8 and H1' also appear broader but are still observable. These findings support the idea of metal ion binding occurring at the single-stranded loop residues but imply low tendency of Mn^{2+} to bind here. C65H5 and T64H6 at the 3' end of dIBS1 as well as G14H1' and H8 of EBS1 are broadened to baseline indicating strong binding near the cleavage site. G13 resonances were not observed in either the absence or the presence of Mn^{2+} and could not be evaluated.

Finally, we performed structure calculations of $[Co(NH_3)_6]^{3+}$ bound to d3'EBS1·dIBS1. Apart from the chemical shift changes that $[Co(NH_3)_6]^{3+}$ binding induces (Figure 7), NOEs between DNA or RNA protons (Table 1) and the 18 protons of the NH_3 ligands can be observed upon binding of the complex to the nucleic acid in [^{1}H,^{1}H]-NOESY spectra. This fact is exploited to localize metal ion binding sites on DNA or RNA molecules (77,93). These NOEs were used to calculate the solution structure of d3'EBS1·dIBS1 with three $[Co(NH_3)_6]^{3+}$-molecules bound. To get a more comprehensive picture of the effect of different metal ions on different parts of d3'EBS1·dIBS1, we mapped the results of Mg^{2+}-, Mn^{2+}- and $[Co(NH_3)_6]^{3+}$ titrations on this structure (Figure 9A). Evidently, the three calculated $[Co(NH_3)_6]^{3+}$ binding sites (large dark blue spheres) coincide well with the protons reacting to the addition of Mg^{2+} (grey spheres) and Mn^{2+} addition (yellow spheres) and with protons that are strongly affected by at least two different metal species (cyan spheres).

Ultimately, three metal ion binding sites of d3'EBS1·dIBS1 can be defined: the first one in the lower part of the RNA stem centered at the G4·C26 base pair and the second and third site in the loop region. Of the latter two, one is located at the stem-loop junction, involving the unpaired bases on both sides of EBS1 and the G19·C59 base pair and the other is formed between dIBS1 and

EBS1, near the 5' end of the EBS1. All the resulting binding sites are situated in the major groove of either the stem or of EBS1·dIBS1. Figure 9A also demonstrates that Mg^{2+}-induced chemical shift changes alone (represented by grey spheres) often coincide well with the effect of other metal ions indicating true binding regions. However, chemical shift changes can also be caused by structural effects on protons in the vicinity of a binding site (94) as it is the case for U9H2' and U7H6 (see arrows in Figure 9A).

The proposed binding sites agree well with the electrostatic surface potential of d3'EBS1·dIBS1 (see arrows in Figure 9B and 9C). In the case of the loop binding site close to G13·C65 the electrostatic surface potential map reveals a small, negatively charged cavity that is formed between dIBS1 and EBS1. Probably, the Mg^{2+}, attracted by the negative charge, binds further inside this cavity and interacts with N7 of G13 or G14. This possibility is not reflected by the calculated position of the $[Co(NH_3)_6]^{3+}$ ion which is probably due to the complex being too big to enter the tunnel. In contrast to Co^{3+} in $[Co(NH_3)_6]^{3+}$, both Mg^{2+} and Mn^{2+} can shed their water ligands partly or entirely and make innersphere contacts to nucleic acid ligands. Importantly, addition of the much smaller Mn^{2+} ion has an effect on G14 protons while $[Co(NH_3)_6]^{3+}$ ion addition does not, which supports the concept of Mg^{2+} and Mn^{2+} binding further inside the cavity than $[Co(NH_3)_6]^{3+}$.

DISCUSSION

In this study, we present the first solution structure of an EBS1·dIBS1 hybrid representing the recognition and cleavage site of a group IIB intron and a DNA target. In the absence of their binding partner, dIBS1 is entirely unstructured and d3'EBS1 forms a stable hairpin with an unstructured loop region (55). Upon dIBS1 binding to EBS1, the two form a short hybrid helix whose position relative to the stem is determined by the stacking interactions and putative hydrogen bonds between the single-stranded nucleotides surrounding EBS1. Due to EBS1·dIBS1 helix formation, the loop backbone is no longer flexible and is forced to assume a sharp turn between the first nucleotide of EBS1 and U12/δ base. These structural features are highly similar to those of the analogous RNA·RNA interaction of d3'EBS1·IBS1 that was previously solved in our group (Figure 10, compare Figure 10A and Figure 5). Based on this structure, we argued that the position of EBS1 in the loop and the length of the loop forcibly leads to formation of this turn, upon IBS1 binding and hence to adjusting the scissile bond at the 3'-OH of C65 in a defined position well accessible for the other active site components. In this paper we demonstrate that also the dIBS1 target strand will induce the same characteristic kinked structure of the recognition complex although it has a much weaker affinity and different conformation when bound to EBS1 than the RNA target. Also in the crystal structure of a substrate-bound group IIC intron (54), a very similar turn is observed between δ and the first EBS1 nucleotide and δ' and IBS1 bind from different sides, thus supporting a general relevance of the kink for the active site architecture. The helical geometries of EBS1·dIBS1 and EBS1·IBS1 are very different on the side of the target strand. This difference strongly suggests that the specific geometry of EBS1·(d)IBS1 is not relevant for cleavage site recognition, with the exception of C65. At C65, the cleavage site, the structure of dIBS1 and IBS1 is more similar. C65 in dIBS1 has the, for DNA unusual C3'-*endo* sugar pucker, which it naturally has in IBS1 RNA. Probably, this is meaningful for the alignment of the scissile bond in the active centre and the coordination of the catalytic Mg^{2+} ions and thus it must be the same in both DNA and RNA targets. The importance of the conformation of C65 is underlined by the crystal structure of the group IIC intron of O. *iheyensis*, in which two metal ions are coordinated in the active site between the backbone of the 3'-terminus of IBS1 and the catalytically relevant nucleotides of DV (54), in a position and mutual distance that would allow catalysis by a two-metal ion mechanism (43).

The RNA·RNA and the RNA·DNA contacts differ in the relative orientation of the EBS1·(d)IBS1 helices to the d3' stem (Figure 10B and 10C); EBS1·IBS1 is more tilted than EBS1·dIBS1 resulting in a different position of the cleavage site with respect to the stem (Figure 10C). One possible interpretation is that the hybrid helix, being more flexible than the homoduplex, can arrange in a way that maximizes stacking onto the stem helix, while the RNA·RNA interaction is too rigid for this. Within the full-length intron,

however, this difference might be of little consequence, since a multitude of interactions such as the δ-δ' base pair (Figure 1C) and tertiary contacts between DV and EBS1·IBS1 (95) as well as contacts between the target strand and the auxiliary protein components of the IEP influence the exact cleavage site position.

The difference in geometry between the RNA·RNA and the RNA·DNA interaction causes the latter to be markedly less stable. This is well in line with previous studies attesting lower melting temperatures and lower thermodynamic stability to hybrid helices in comparison to RNA·RNA homoduplexes of corresponding sequence (96-98). We could show by SPR measurements that Mg^{2+} concentrations similar to the physiological concentration stabilize both the RNA·DNA and the RNA·RNA interaction strongly without altering the overall helical geometry. Control experiments did not reveal any changes in the fold or the flexibility of the unbound d3'EBS1 loop upon Mg^{2+} addition (55). This is in line with the observation that Mg^{2+} has little influence on the association of EBS1 and dIBS1. In contrast to this, Mg^{2+} strongly decreases the dissociation rate constant. Probably Mg^{2+} helps to prevent dissociation of the exon-intron recognition complex until all active site components have been assembled or even throughout the cleavage reaction. In the following, the metal-ion binding sites relevant for this stabilization will be evaluated. At the K^+ and Mg^{2+} concentrations used, it is probable that also diffuse Mg^{2+} ions play a role in the stabilization of EBS1·(d)IBS1 (99), a detailed quantification of their influence, however, is beyond the scope of this work. We thus focus the discussion on the site-bound Mg^{2+} ions.

The binding site found in the d3' RNA stem of d3'EBS1 shows a preference for $[Co(NH_3)_6]^{3+}$ or hydrated Mg^{2+} as for almost all protons 2 mM $[Co(NH_3)_6]^{3+}$ cause stronger chemical shift changes than 3 mM Mg^{2+} (Figure 7A) and a wealth of NOE correlations to $[Co(NH_3)_6]^{3+}$ are observed. Such outersphere binding sites in the major groove are regularly found in RNA (86). Possibly, this binding site contributes to stability, for example by making the d3' stem more rigid. However, the two metal ion binding sites in the loop region (Figure 9A) directly involve EBS1 and dIBS1 nucleotides and thus seem more relevant for the affinity of d3'EBS1·dIBS1 in the presence of Mg^{2+}. These are located in the major groove at the two termini of EBS1·dIBS1. Neither binding site shows a clear preference for inner- or outersphere binding. In general, the NMR and SPR data do not provide an exact characterization of the mode of interaction (100,101) of the Mg^{2+} ion with each binding site, since all three metal ions tested are able to interact with each binding site and since both Mg^{2+} and $[Co(NH_3)_6]^{3+}$ efficiently enhance affinity of dIBS1 for d3'EBS1.

Metal ion binding at the 5'-end of dIBS1 may reduce the flexibility of the unpaired nucleotides and contribute to stabilize this end of the EBS1·dIBS1 helix, by accepting ligand atoms from C59, G19 and the unpaired nucleotides surrounding them. In the second loop binding site, located between EBS1 and dIBS1 close to the G13·C65 and G14·T64 base pairs, Mn^{2+} and Mg^{2+} seem to be able to bind deeper inside the tunnel-shaped major groove than $[Co(NH_3)_6]^{3+}$. This indicates that a Mg^{2+} ion might be able to move slightly within this binding region by exchanging some of its hydration shell with nucleic acid ligands. Such partial innersphere coordination is well in line with crystal structures of RNAs in general, which show that the vast majority of Mg^{2+} ions are partially dehydrated (102,103). In general, the combination of the kink in the sugar phosphate backbone at G13 and the short and tunnel-shaped major groove of EBS1·dIBS1 seems ideal to attract metal ions as it provides a suitable shape and accumulates negative charge in a small region. The G9·U21 wobble pair closing the loop, which is known for its affinity towards metal ions, completes this binding platform.

Mg^{2+} titrations of d3'EBS1·IBS1 indicate that Mg^{2+} binds to the same regions in both constructs (55). This means that the overall structure described above, which is common to the RNA·RNA and the RNA·DNA contact (Figure 10B-E) is much more relevant to attract metal ions than the specific geometry of the EBS1·(d)IBS1 helix including the exact width of the major groove, which is different (Figure 10D and 10E). Moreover, this structure is supposed to form independently of the exact sequences of dIBS1 and EBS1, provided the length and position of EBS1 in the d3' loop are suitable (see above and (55)). The hypothesis of equivalent Mg^{2+} binding to different EBS1·(d)IBS1 sequences is tentatively supported by the observation that also the wild

type sequences of d3'EBS1·IBS1 and d3'EBS1·dIBS1 show much higher affinities in the presence of low milimolar Mg^{2+} concentrations. However, localization of these binding sites and structure determination is impeded by the low affinity of the wild type recognition complex EBS1·(d)IBS1.

It thus is reasonable to assume that, similar structural features as described above are used by different group II introns to attract stabilizing metal ions to the EBS1·IBS1 complex. In the case of the *O. iheyensis* group IIC intron, a binding site for divalent metal ions is found in the d3' stem major groove near the single-stranded nucleotides framing EBS1 (54). Furthermore, G·U wobble base pairs (see above) are found at different positions within EBS1·IBS1 (as in *Rm*Int1 (104), *Sc*B1 and *So*PETD (17) and *Ec*I5 introns (105)) or at the final base pair of the d3' stem (as in *Pl*.LSU/2 (106), *Ll*.LtrB (107) introns) in other group II introns supporting the idea that metal ion binding in EBS1·IBS1 is a common feature.

It has been shown both in bacterial and eukaryotic cells that the efficiency of retrohoming is strongly coupled to the Mg^{2+} concentration in the cell (47,48). In fact, the lower Mg^{2+} concentration of the eukaryotic cell limits the retrohoming efficiency of group II introns that are of bacterial origin. Probably group II introns residing in eukaryotic genomes have evolved to make optimal use of the available Mg^{2+} for example, by promoting structures such as the one of the cleavage site recognition complex described herein.

ACCESSION NUMBER

Structure coordinates and NMR restraint files have been deposited to the protein Data Bank (PDB) with the accession code 2M1V. Chemical shifts have been deposited to BioMagResBank (BMRB) with the accession code 18881.

REFERENCES

1. Peebles, C. L., Perlman, P. S., Mecklenburg, K. L., Petrillo, M. L., Tabor, J. H., Jarrell, K. A., and Cheng, H. L. (1986) A self-splicing RNA excises an intron lariat. *Cell* **44**, 213-223
2. Schmelzer, C., and Schweyen, R. J. (1986) Self-splicing of group II introns in vitro: Mapping of the branch point and mutational inhibition of lariat formation. *Cell* **46**, 557-565
3. van der Veen, R., Arnberg, A. C., van der Horst, G., Bonen, L., Tabak, H. F., and Grivell, L. A. (1986) Excised group II introns in yeast mitochondria are lariats and can be formed by self-splicing in vitro. *Cell* **44**, 225-234
4. Yang, J., Zimmerly, S., Perlman, P. S., and Lambowitz, A. M. (1996) Efficient integration of an intron RNA into double-stranded DNA by reverse splicing. *Nature* **381**, 332-335
5. Augustin, S., Müller, M. W., and Schweyen, R. J. (1990) Reverse self-splicing of group II intron RNAs in vitro. *Nature* **343**, 383-386
6. Mörl, M., Niemer, I., and Schmelzer, C. (1992) New reactions catalyzed by a group II intron ribozyme with RNA and DNA substrates. *Cell* **70**, 803-810
7. Lambowitz, A. M., and Zimmerly, S. (2011) Group II Introns: Mobile Ribozymes that Invade DNA. *Cold Spring Harbor Perspectives in Biology* **3**, 1-19
8. Séraphin, B., Faye, G., Hatat, D., and Jacq, C. (1992) The yeast mitochondrial intron aI5α: associated endonuclease activity and in vivo mobility. *Gene* **113**, 1-8
9. Matsuura, M., Saldanha, R., Ma, H., Wank, H., Yang, J., Mohr, G., Cavanagh, S., Dunny, G. M., Belfort, M., and Lambowitz, A. M. (1997) A Bacterial Group II Intron Encoding Reverse Transcriptase, Maturase, and DNA Endonuclease Activities: Biochemical Demonstration of Maturase Activity and Insertion of New Genetic Information Within the Intron. *Genes Dev.* **11**, 2910-2924
10. Saldanha, R., Chen, B., Wank, H., Matsuura, M., Edwards, J., and Lambowitz, A. M. (1999) RNA and Protein Catalysis in Group II Intron Splicing and Mobility Reactions Using Purified Components. *Biochemistry* **38**, 9069-9083

11. Curcio, M. J., and Belfort, M. (1996) Retrohoming: cDNA-Mediated Mobility of Group II Introns Requires a Catalytic RNA. *Cell* **84**, 9-12
12. Sharp, P. A. (1985) On the origin of RNA splicing and introns. *Cell* **42**, 397-400
13. Cavalier-Smith, T. (1991) Intron phylogeny: a new hypothesis. *Trends Genet.* **7**, 145-148
14. Mattick, J. S., and Gagen, M. J. (2001) The evolution of controlled multitasked gene networks: the role of introns and other noncoding RNAs in the development of complex organisms. *Mol. Biol. Evol.* **18**, 1611-1630
15. Martin, W., and Koonin, E. V. (2006) Introns and the origin of nucleus-cytosol compartmentalization. *Nature* **440**, 41-45
16. Michel, F., and Feral, J. (1995) Structure and Activities of Group II Introns. *Annu. Rev. Biochem.* **64**, 435-461
17. Jacquier, A., and Michel, F. (1987) Multiple exon-binding sites in class II self-splicing introns. *Cell* **50**, 17-29
18. Costa, M., Michel, F., and Westhof, E. (2000) A three-dimensional perspective on exon binding by a group II self-splicing intron. *EMBO J.* **19**, 5007-5018
19. Lencastre, A. d., Hamill, S., and Pyle, A. M. (2005) A single active-site region for a group II intron. *Nat. Struct. Mol. Biol.* **12**, 626-627
20. Qin, P. Z., and Pyle, A. M. (1998) The architectural organization and mechanistic function of group II intron structural elements. *Curr. Opin. Struct. Biol.* **8**, 301-308
21. Michel, F., Umesono, K., and Ozeki, H. (1989) Comparative and functional anatomy of group II catalytic introns - a review. *Gene* **82**, 5-30
22. Xiang, Q., Qin, P. Z., Michels, W. J., Freeland, K., and Pyle, A. M. (1998) Sequence Specificity of a Group II Intron Ribozyme: Multiple Mechanisms for Promoting Unusually High Discrimination against Mismatched Targets. *Biochemistry* **37**, 3839-3849
23. Guo, H., Karberg, M., Long, M., Jones, J. P., III, Sullenger, B., and Lambowitz, A. M. (2000) Group II introns designed to insert into therapeutically relevant DNA target sites in human cells. *Science* **289**, 452-457
24. Mohr, G., Smith, D., Belfort, M., and Lambowitz, A. M. (2000) Rules for DNA target-site recognition by a lactococcal group II intron enable retargeting of the intron to specific DNA sequences. *Genes Dev.* **14**, 559-573
25. Qin, P. Z., and Pyle, A. M. (1999) Antagonistic substrate binding by a group II intron ribozyme. *J. Mol. Biol.* **291**, 15-27
26. Perutka, J., Wang, W., Goerlitz, D., and Lambowitz, A. M. (2004) Use of Computer-designed Group II Introns to Disrupt Escherichia coli DExH/D-box Protein and DNA Helicase Genes. *J. Mol. Biol.* **336**, 421-439
27. Qin, P. Z., and Pyle, A. M. (1997) Stopped-Flow Fluorescence Spectroscopy of a Group II Intron Ribozyme Reveals that Domain 1 Is an Independent Folding Unit with a Requirement for Specific Mg^{2+} Ions in the Tertiary Structure. *Biochemistry* **36**, 4718-4730
28. Su, L. J., Waldsich, C., and Pyle, A. M. (2005) An obligate intermediate along the slow folding pathway of a group II intron ribozyme. *Nucleic Acids Res.* **33**, 6674-6687
29. Pyle, A. M., Fedorova, O., and Waldsich, C. (2007) Folding of group II introns: a model system for large, multidomain RNAs? *Trends Biochem. Sci.* **32**, 138-145
30. Koch, J. L., Boulanger, S. C., Dib-Hajj, S. D., Hebbar, S. K., and Perlman, P. S. (1992) Group II introns deleted for multiple substructures retain self-splicing activity. *Mol. Cell. Biol.* **12**, 1950-1958
31. Michels, W. J., Jr., and Pyle, A. M. (1995) Conversion of a Group II Intron into a New Multiple-Turnover Ribozyme that Selectively Cleaves Oligonucleotides: Elucidation of Reaction Mechanism and Structure/Function Relationships. *Biochemistry* **34**, 2965-2977

32. Sigel, R. K. O., and Pyle, A. M. (2007) Alternative roles for metal ions in enzyme catalysis and the implications for ribozyme chemistry. *Chem. Rev.* **107**, 97-113
33. Schnabl, J., and Donghi, D. (2011) Multiple Roles of Metal Ions in Large Ribozymes. *Met. Ions Life Sci.* **9**, 197-234
34. Sigel, R. K. O. (2005) Group II Intron Ribozymes and Metal Ions – A Delicate Relationship. *Eur. J. Inorg. Chem.* **2005**, 2281-2292
35. Fedor, M. J. (2002) The role of metal ions in RNA catalysis. *Curr. Opin. Struct. Biol.* **12**, 289-295
36. Swisher, J. F., Su, L. J., Brenowitz, M., Anderson, V. E., and Pyle, A. M. (2002) Productive folding to the native state by a group II intron ribozyme. *J. Mol. Biol.* **315**, 297-310
37. Steiner, M., Karunatilaka, K. S., Sigel, R. K. O., and Rueda, D. (2008) Single molecule studies of group II intron ribozymes. *Proc. Natl. Acad. Sci. USA* **105**, 13853-13858
38. Sigel, R. K. O., Vaidya, A., and Pyle, A. M. (2000) Metal ion binding sites in a group II intron core. *Nat. Struct. Mol. Biol.* **7**, 1111-1116
39. Erat, M. C., Zerbe, O., Fox, T., and Sigel, R. K. O. (2007) Solution structure of domain 6 from a self-splicing group II intron ribozyme: a Mg^{2+} binding site is located close to the stacked branch adenosine. *ChemBioChem* **8**, 306-314
40. Donghi, D., Pechlaner, m., Finazzo, C., Knobloch, B., and Sigel, R. K. O. (2013) The structural stabilization of the three-way junction by Mg(II) represents the first step in the folding of a group II intron. *Nucleic Acids Res.* **41**, 2489-2504
41. Sigel, H. (1990) Mechanistic aspects of the metal ion promoted hydrolysis of nucleoside 5'-triphosphates (NTPs). *Coord. Chem. Rev.* **100**, 453-539
42. Steitz, T. A., and Steitz, J. A. (1993) A general two-metal-ion mechanism for catalytic RNA. *Proc. Natl. Acad. Sci. U. S. A.* **90**, 6498-6502
43. Gordon, P. M., Fong, R., and Piccirilli, J. A. (2007) A Second Divalent Metal Ion in the Group II Intron Reaction Center. *Chem. Biol.* **14**, 607-612
44. Toor, N., Rajashankar, K., Keating, K. S., and Pyle, A. M. (2008) Structural basis for exon recognition by a group II intron. *Nat. Struct. Mol. Biol.* **15**, 1221-1222
45. Wiesenberger, G., Waldherr, M., and Schweyen, R. J. (1992) The nuclear gene MRS2 is essential for the excision of group II introns from yeast mitochondrial transcripts in vivo. *J. Biol. Chem.* **267**, 6963-6969
46. Gregan, J., Bui, D. M., Pillich, R., Fink, M., Zsurka, G., and Schweyen, R. J. (2001) The mitochondrial inner membrane protein Lpe10p, a homologue of Mrs2p, is essential for magnesium homeostasis and group II intron splicing in yeast. *Molecular & general genetics: MGG* **264**, 773-781
47. Mastroianni, M., Watanabe, K., White, T. B., Zhuang, F., Vernon, J., Matsuura, M., Wallingford, J., and Lambowitz, A. M. (2008) Group II Intron-Based Gene Targeting Reactions in Eukaryotes. *PLoS ONE* **3**, e3121
48. Truong, D. M., Sidote, D. J., Russell, R., and Lambowitz, A. M. (2013) Enhanced group II intron retrohoming in magnesium-deficient Escherichia coli via selection of mutations in the ribozyme core. *Proceedings of the National Academy of Sciences* **110**, E3800-E3809
49. Su, L. J., Qin, P. Z., Michels, W. J., and Pyle, A. M. (2001) Guiding ribozyme cleavage through motif recognition: the mechanism of cleavage site selection by a group II intron ribozyme. *J. Mol. Biol.* **306**, 655-668
50. Erat, M. C., and Sigel, R. K. O. (2008) Divalent metal ions tune the self-splicing reaction of the yeast mitochondrial group II intron Sc.ai5γ. *J. Biol. Inorg. Chem.* **13**, 1025-1036
51. Toor, N., Keating, K. S., Taylor, S. D., and Pyle, A. M. (2008) Crystal structure of a self-spliced group II intron. *Science* **320**, 77-82
52. Wang, J. (2010) Inclusion of weak high-resolution X-ray data for improvement of a group II intron structure. *Acta crystallographica. Section D, Biological crystallography* **66**, 988-1000

53. Chan, R. T., Robart, A. R., Rajashankar, K. R., Pyle, A. M., and Toor, N. (2012) Crystal structure of a group II intron in the pre-catalytic state. *Nat. Struct. Mol. Biol.* **19**, 555-557
54. Marcia, M., and Pyle, Anna M. (2012) Visualizing Group II Intron Catalysis through the Stages of Splicing. *Cell* **151**, 497-507
55. Kruschel, D., Skilandat, M., and Sigel, R. K. O. (2014) NMR structure of the 5'-splice site in the group IIB intron Sc.ai5gamma – conformational requirements for exon-intron recognition. *RNA*
56. Milligan, J. F., Uhlenbeck, O. C., and James E. Dahlberg, J. N. A. (1989) Synthesis of small RNAs using T7 RNA polymerase. *Methods Enzymol.* **180**, 51-62
57. Kruschel, D., and Sigel, R. K. O. (2008) Divalent metal ions promote the formation of the 5'-splice site recognition complex in a self-splicing group II intron. *J. Inorg. Biochem.* **102**, 2147-2154
58. Gallo, S., Furler, M., and Sigel, R. K. O. (2005) In vitro transcription and purification of RNAs of different size. *Chimia* **59**, 812-816
59. Glasoe, P. K., and Long, F. A. (1960) Use of glass electrodes to measure acidities in deuterium oxide. *J. Phys. Chem.* **64**, 188-190
60. Breeze, A. L. (2000) Isotope-filtered NMR methods for the study of biomolecular structure and interactions. *Prog. Nucl. Magn. Reson. Spectrosc.* **36**, 323-372
61. Markley, J. L., Bax, A., Arata, Y., Hilbers, C. W., Kaptein, R., Sykes, B. D., Wright, P. E., and Wüthrich, K. (1998) Recommendations for the presentation of NMR structures of proteins and nucleic acids. IUPAC-IUBMB-IUPAB Inter-Union Task Group on the Standardization of Data Bases of Protein and Nucleic Acid Structures Determined by NMR Spectroscopy. *J. Biomol. NMR* **12**, 1-23
62. Tjandra, N., and Bax, A. (1997) Measurement of Dipolar Contributions to $^{1}J_{CH}$ Splittings from Magnetic-Field Dependence of *J* Modulation in Two-Dimensional NMR Spectra. *J. Magn. Reson.* **124**, 512-515
63. Vranken, W. F., Boucher, W., Stevens, T. J., Fogh, R. H., Pajon, A., Llinas, M., Ulrich, E. L., Markley, J. L., Ionides, J., and Laue, E. D. (2005) The CCPN data model for NMR spectroscopy: Development of a software pipeline. *Proteins: Struct., Funct., Bioinf.* **59**, 687-696
64. Güntert, P., Mumenthaler, C., and Wüthrich, K. (1997) Torsion angle dynamics for NMR structure calculation with the new program DYANA. *J. Mol. Biol.* **273**, 283-298
65. Varani, G., Aboul-ela, F., and Allain, F. H. T. (1996) NMR investigation of RNA structure. *Prog. Nucl. Magn. Reson. Spectrosc.* **29**, 51-127
66. Brünger, A. T., Adams, P. D., Clore, G. M., DeLano, W. L., Gros, P., Grosse-Kunstleve, R. W., Jiang, J. S., Kuszewski, J., Nilges, M., Pannu, N. S., Read, R. J., Rice, L. M., Simonson, T., and Warren, G. L. (1998) Crystallography & NMR System: A New Software Suite for Macromolecular Structure Determination. *Acta Crystallogr. Sect. D Biol. Crystallogr.* **54**, 905-921
67. Brünger, A. T. (2007) Version 1.2 of the Crystallography and NMR system. *Nat. Protoc.* **2**, 2728-2733
68. Schwieters, C. D., Kuszewski, J. J., Tjandra, N., and Marius Clore, G. (2003) The Xplor-NIH NMR molecular structure determination package. *J. Magn. Reson.* **160**, 65-73
69. Schwieters, C. D., Kuszewski, J. J., and Marius Clore, G. (2006) Using Xplor-NIH for NMR molecular structure determination. *Prog. Nucl. Magn. Reson. Spectrosc.* **48**, 47-62
70. Zweckstetter, M. (2008) NMR: prediction of molecular alignment from structure using the PALES software. *Nat. Protoc.* **3**, 679-690
71. Clore, G. M., Gronenborn, A. M., and Tjandra, N. (1998) Direct structure refinement against residual dipolar couplings in the presence of rhombicity of unknown magnitude. *J. Magn. Reson.* **131**, 159-162
72. Koradi, R., Billeter, M., and Wüthrich, K. (1996) MOLMOL: A program for display and analysis of macromolecular structures. *J. Mol. Graph.* **14**, 51-55

73. Dolinsky, T. J., Nielsen, J. E., McCammon, J. A., and Baker, N. A. (2004) PDB2PQR: an automated pipeline for the setup of Poisson-Boltzmann electrostatics calculations. *Nucleic Acids Res.* **32**, W665-W667
74. Dolinsky, T. J., Czodrowski, P., Li, H., Nielsen, J. E., Jensen, J. H., Klebe, G., and Baker, N. A. (2007) PDB2PQR: expanding and upgrading automated preparation of biomolecular structures for molecular simulations. *Nucleic Acids Res.* **35**, W522-W525
75. Lu, X.-J., and Olson, W. K. (2003) 3DNA: A Software Package for the Analysis, Rebuilding and Visualization of Three-Dimensional Nucleic Acid Structures. *Nucleic Acids Res.* **31**, 5108-5121
76. Zheng, G., Lu, X. J., and Olson, W. K. (2009) Web 3DNA--a web server for the analysis, reconstruction, and visualization of three-dimensional nucleic-acid structures. *Nucleic Acids Res.* **37**, W240-W246
77. Kieft, J. S., and Tinoco Jr, I. (1997) Solution structure of a metal-binding site in the major groove of RNA complexed with cobalt (III) hexammine. *Structure* **5**, 713-721
78. Horton, N. C., and Finzel, B. C. (1996) The Structure of an RNA/DNA Hybrid: A Substrate of the Ribonuclease Activity of HIV-1 Reverse Transcriptase. *J. Mol. Biol.* **264**, 521-533
79. Fedoroff, O. Y., Salazar, M., and Reid, B. R. (1993) Structure of a DNA : RNA Hybrid Duplex: Why RNase H Does Not Cleave Pure RNA. *J. Mol. Biol.* **233**, 509-523
80. Xiong, Y., and Sundaralingam, M. (2000) Crystal Structure of a DNA·RNA Hybrid Duplex with a Polypurine RNA R(gaagaagag) and a Complementary Polypyrimidine DNA d(CTCTTCTTC). *Nucleic Acids Res.* **28**, 2171-2176
81. Hung, S. H., Yu, Q., Gray, D. M., and Ratliff, R. L. (1994) Evidence from CD spectra that d(purine)·r(pyrimidine) and r(purine)·d(pyrimidine) hybrids are in different structural classes. *Nucleic Acids Res.* **22**, 4326-4334
82. Roberts, R. W., and Crothers, D. M. (1992) Stability and properties of double and triple helices: dramatic effects of RNA or DNA backbone composition. *Science* **258**, 1463-1466
83. Cross, C. W., Rice, J. S., and Gao, X. (1997) Solution Structure of an RNA·DNA Hybrid Duplex Containing a 3'-Thioformacetal Linker and an RNA A-Tract. *Biochemistry* **36**, 4096-4107
84. Bradshaw, P. C., and Pfeiffer, D. R. (2006) Release of Ca^{2+} and Mg^{2+} from yeast mitochondria is stimulated by increased ionic strength. *BMC Biochem.* **7**
85. Grubbs, R. D. (2002) Intracellular magnesium and magnesium buffering. *BioMetals* **15**, 251-259
86. Rowinska-Zyrek, M., Skilandat, M., and Sigel, R. K. O. (2013) Hexaamminecobalt(III) - Probing Metal Ion Binding Sites in Nucleic Acids by NMR. *Z. Anorg. Allg. Chem.* **639**, 1313-1320
87. Hampel, K. J., Walter, N. G., and Burke, J. M. (1998) The Solvent-Protected Core of the Hairpin Ribozyme-Substrate Complex. *Biochemistry* **37**, 14672-14682
88. Kurz, J. C., and Fierke, C. A. (2002) The Affinity of Magnesium Binding Sites in the Bacillus subtilis RNase P·Pre-tRNA Complex Is Enhanced by the Protein Subunit *Biochemistry* **41**, 9545-9558
89. Erat, M. C., and Sigel, R. K. O. (2007) Determination of the Intrinsic Affinities of Multiple Site-Specific Mg^{2+} Ions Coordinated to Domain 6 of a Group II Intron Ribozyme. *Inorg. Chem.* **46**, 11224-11234
90. Hurd, R. E., Azhderian, E., and Reid, B. R. (1979) Paramagnetic ion effects on the nuclear magnetic resonance spectrum of transfer ribonucleic acid: assignment of the 15-48 tertiary resonance. *Biochemistry* **18**, 4012-4017
91. Erat, M. C., and Sigel, R. K. O. (2011) Methods to detect and characterize metal ion binding sites in RNA. *Met Ions Life Sci* **9**, 37-100
92. Allain, F. H. T., and Varani, G. (1995) Divalent metal ion binding to a conserved wobble pair defining the upstream site of cleavage of group I self-splicing introns. *Nucleic Acids Res.* **23**, 341-350
93. Robinson, H., and Wang, A. H. J. (1996) Neomycin, Spermine and Hexaamminecobalt(III) Share Common Structural Motifs in Converting B- to A-DNA. *Nucleic Acids Res.* **24**, 676-682

94. Pechlaner, M., and Sigel, R. K. O. (2012) Characterization of metal ion-nucleic acid interactions in solution. *Met Ions Life Sci* **10**, 1-42
95. Costa, M., and Michel, F. (1999) Tight binding of the 5' exon to domain I of a group II self-splicing intron requires completion of the intron active site. *EMBO J.* **18**, 1025-1037
96. Hall, K. B., and McLaughlin, L. W. (1991) Thermodynamic and structural properties of pentamer DNA·DNA, RNA·RNA and DNA·RNA duplexes of identical sequence. *Biochemistry* **30**, 10606-10613
97. Ratmeyer, L., Vinayak, R., Zhong, Y. Y., Zon, G., and Wilson, W. D. (1994) Sequence Specific Thermodynamic and Structural Properties for DNA·RNA Duplexes. *Biochemistry* **33**, 5298-5304
98. Lesnik, E. A., and Freier, S. M. (1995) Relative Thermodynamic Stability of DNA, RNA, and DNA:RNA Hybrid Duplexes: Relationship with Base Composition and Structure. *Biochemistry* **34**, 10807-10815
99. Bai, Y., Greenfeld, M., Travers, K. J., Chu, V. B., Lipfert, J., Doniach, S., and Herschlag, D. (2007) Quantitative and Comprehensive Decomposition of the Ion Atmosphere around Nucleic Acids. *J. Am. Chem. Soc.* **129**, 14981-14988
100. Draper, D. E., Grilley, D., and Soto, A. M. (2005) Ions and RNA Folding. *Annu. Rev. Biophys. Biomol. Struct.* **34**, 221-243
101. Bowman, J. C., Lenz, T. K., Hud, N. V., and Williams, L. D. (2012) Cations in charge: magnesium ions in RNA folding and catalysis. *Curr. Opin. Struct. Biol.* **22**, 262-272
102. Schnabl, J., Suter, P., and Sigel, R. K. O. (2012) MINAS--a database of Metal Ions in Nucleic AcidS. *Nucleic Acids Res.* **40**, D434-D438
103. Freisinger, E., and Sigel, R. K. O. (2007) From nucleotides to ribozymes – A comparison of their metal ion binding properties. *Coord. Chem. Rev.* **251**, 1834-1851
104. Barrientos-Durán, A., Chillón, I., Martínez-Abarca, F., and Toro, N. (2011) Exon sequence requirements for excision in vivo of the bacterial group II intron RmInt1. *BMC Mol. Biol.* **12:24**
105. Zhuang, F., Karberg, M., Perutka, J., and Lambowitz, A. M. (2009) EcI5, a group IIB intron with high retrohoming frequency: DNA target site recognition and use in gene targeting. *RNA* **15**, 432-449
106. Costa, M., Christian, E. L., and Michel, F. (1998) Differential chemical probing of a group II self-splicing intron identifies bases involved in tertiary interactions and supports an alternative secondary structure model of domain V. *RNA* **4**, 1055-1068
107. Mills, D. A., McKay, L. L., and Dunny, G. M. (1996) Splicing of a group II intron involved in the conjugative transfer of pRS01 in lactococci. *J. Bacteriol.* **178**, 3531-3538

Acknowledgements - We thank Dr. Jens Sobek and Dr. Stefan Schauer at the Functional Genomics Centre Zurich, Switzerland for support with the SPR experiments. We thank Dr. Maria Pechlaner and Dr. Silke Johannsen for their helpful comments on the manuscript.

FOOTNOTES:

***** This work was generously supported by the Swiss National Science Foundation [200021-124834 to RKOS], the University of Zurich, and the European Research Commission (ERC starting grant MIRNA to RKOS), for which we are very grateful.

[1] To whom correspondence should be addressed: Roland K. O. Sigel, Department of Chemistry, University of Zurich, Winterthurerstrasse 190, CH-8057 Zurich, Switzerland
Tel: +41 44 6354652; Fax: +41 44 6356802; Email: roland.sigel@chem.uzh.ch

[2] Other H1'-H2' or H3'-H4' TOCSY correlations could not be reliably analyzed due to line-broadening.

FIGURE LEGENDS

Figure 1. Location and secondary structure of EBS1 and dIBS1. (A) Scheme of the proposed secondary structure of a group IIB intron. Base pairs between EBS1-3 (purple) and exonic IBS1-3 (green) as well as the δ and δ' bases (orange) mediate correct recognition of the 5' and 3' exon both in splicing and reverse splicing events. The six domains of the intron (DI-DVI) and the four main branches of DI (Ia-Id) are labeled. Sites of intron-catalyzed cleavage are marked with black arrows. (B) d3'EBS1·dIBS1, the RNA·DNA hybrid construct used in this study. The sequences of nucleotide 5-25 of the RNA (d3'EBS1) containing EBS1 (purple) and of dIBS1 DNA (green) are derived from the *Sc*.ai5γ intron found in the *cox1* gene of *S. cerevisiae* mitochondria The base pairs marked with light green/dark purple letters were mutated from A·T to G·C for the sake of stability (57). The nucleotides 1-4 and 26-29 (boxed) are added to the wild type sequence. (C) The spatial arrangement of the EBS·dIBS and δ-δ' base pairs ensures binding of both exons in the correct orientation for cleavage. Interactions are exemplified for a double-stranded DNA target (grey).

Figure 2. dIBS1 adopts a helical structure upon binding to EBS1. (A) [^{1}H,^{1}H]-NOESY of the exchangeable (imino) protons (5 °C in 90 % H_2O/10 % D_2O). Presence of diagonal peaks for all G,T and U residues in the IBS1·EBS1 helix and cross peaks between neighboring dIBS1 residues (connected by green lines) and between EBS1 and IBS1 residues prove base pair formation between the two strands. (B) Superposition of the *F1,F2*-[^{13}C,^{15}N]-filtered [^{1}H,^{1}H]-NOESY (colored) containing only peaks of IBS1 protons and the normal [^{1}H,^{1}H]-NOESY (grey). Intense sequential cross peaks between dIBS1 residues (labeled in boldface and connected by lines) indicate that dIBS1 assumes a stable fold. Cross peaks between proton resonances of dIBS1 C59 and EBS1 proton resonances are labeled. Spectra were recorded at 25 °C in D_2O.

Figure 3. [^{1}H,^{1}H]-NOESY spectrum of d3'EBS1·dIBS1 showing cross peaks between dIBS1 H2'/H2" and H6/H8 protons of dIBS1. On the right, the residue of the H6/H8 resonance is indicated. The intraresidue H2"-H6/8 cross peaks are labelled in black, the interresidue H2"-H6/8 cross peaks are labelled in grey. The sequential walk between intra- and inter-residue H2"-H6/8 cross peaks is shown as a black line. In a standard B-form conformation cross-peak pattern, the H2'(i)-H6/8(i) (intraresidue) cross peak is more intense than the H2"(i)-H6/8(i) cross peak whereas the H2"(i-1)-H6/8(i) (interresidue) cross peak is more intense than H2'(i-1)-H6/8(i). The fact that no such pattern is observed rules out a stable B-form conformation of the DNA and the rather broad appearance of the peaks points out flexibility of dIBS1. The spectrum was recorded in D_2O at 25 °C.

Figure 4. [^{1}H,^{1}H]-TOCSY spectrum of d3'EBS1·dIBS1. An intense H3'-H4' and a weak or absent H1'-H2' cross peak in the TOCSY indicates a C3'-*endo* sugar pucker, found in A-form DNA and RNA while the opposite situation is characteristic of a C2'-*endo* pucker typical for B-DNA. All H3'-H4' cross peaks belonging to dIBS1, have similar and intermediate intensities except for C65H4'-H3', which is more intense pointing out a C3'-*endo* conformation. For comparison, the very intense H2'-H1' cross peaks of A10, U11 and U12 corresponding to a C2'-*endo* conformation are shown, other RNA H2'-H1' cross peaks that would be located in this spectral region are invisible due to the stem nucleotides having regular C3'-*endo* sugar pucker. The spectrum was recorded on a sample containing partially deuterated d3'EBS1 and natural abundance dIBS1 in D_2O at 25 °C.

Figure 5. Solution structure of d3'EBS1·dIBS1. EBS1 nucleotides are colored purple, dIBS1 nucleotides are shown in green, nucleotides in single-stranded regions are shown in light grey, residues of the helical stem are shown in dark grey. The figure was prepared with MOLMOL (72). (A) The 18 conformers of lowest energy superimposed by their heavy atoms. Hydrogen atoms are omitted for simplicity. (B) The EBS1·dIBS1 helix. While the EBS1 backbone traces are well converged, the dIBS1 backbone trajectory differs between the 18 conformers. (C) Close-up of the kink in the RNA backbone between U12 and G13. The sharp turn of the backbone moves G13 far from U12 and exposes it to the solvent on the 5'-side. (D)

Two examples of the conformation of the single-stranded nucleotides that link EBS1·dIBS1 with the helical stem. A10 and A20 stabilize the junction of the stem helix and the EBS1·dIBS1 hybrid by stacking interactions. U11 and U12 show largest conformational variability among the d3'EBS1 nucleotides.

Figure 6. Sensorgrams of dIBS1 to d3'EBS1 binding in the presence of different concentrations of Mg^{2+}. The legend is sorted in the order of injection of the different dIBS1 concentrations. The injection starts at t = 0 s and ends at t = 60 s. All experiments were carried out at 15 °C . In presence of 5 mM Mg^{2+}, an additional injection with 0.25 µM dIBS1 was added to sample the concentration range around the lowered K_D better. The presence of increasing amounts of Mg^{2+} markedly slows down the dissociation of dIBS1 (t > 60 s) from d3'EBS1. Note the decreasing total maximum RU value (RU_{max}) reached in 1 and 5 mM Mg^{2+} and the lower RU_{max} reached in the second injection of 4.0 µM dIBS1 relative to the first injection, which indicate Mg^{2+}-enhanced self-cleavage of d3'EBS1 from biotin. The enhanced dissociation rate of IBS1 from d3'EBS1 is evident from the much slower decrease in response units after the injection end at 60 s in the presence of Mg^{2+}.

Figure 7. Chemical shift changes Δδ induced by Mg^{2+}- and $[Co(NH_3)_6]^{3+}$ addition of (A) RNA proton resonances of the d3' stem and (B) RNA and DNA proton resonances of the loop region and EBS1·dIBS1. Displayed are the chemical shift differences between 3 mM and 0 mM Mg^{2+} (dark grey) and between 2 mM and 0 mM $[Co(NH_3)_6]^{3+}$ (light grey). Only resonances with a chemical shift difference of ≥ 0.02 ppm for either 2 mM Mg^{2+} or 3 mM $[Co(NH_3)_6]^{3+}$ were taken into account. For G13 there are no data in the presence of Mg^{2+} (*) as the peaks were not detectable in the spectra. Residues are ordered from left to right as illustrated on the right-hand side of the plot (see numbering of hairpin in Figure 1B).

Figure 8. Mn^{2+} binding causes line-broadening of RNA and DNA protons. Superposition of the [^{1}H,^{1}H]-NOESY spectrum (25 °C in D_2O) recorded in the absence of Mn^{2+} (red) and in the presence of 60 µM Mn^{2+} (black), respectively. Unless otherwise noted, all labeled resonances in F1 belong to H6 or H8 protons and resonances in F2 to H1' protons. Peaks that have broadened below the detection threshold due to the presence of Mn^{2+} appear in red. Some cross peaks like A20H1'-H8 and A20H8-G19H1' display severe broadening but are still detectable indicating a weaker interaction of the proton and the Mn^{2+} ion.

Figure 9. Proposed metal ion binding sites of d3'EBS1·IBS1 and their relation to the electrostatic surface potential. (A) Metal ion binding regions defined by titration experiments. The effect of the three different metal ions Mg^{2+}, Mn^{2+} and $[Co(NH_3)_6]^{3+}$ are mapped onto the structure of d3'EBS1. Protons suffering only complete line broadening at 60 µM Mn^{2+} are shown as yellow spheres. Protons displaying only NOEs to $[Co(NH_3)_6]^{3+}$ protons are shown as blue spheres. Protons experiencing only chemical shift differences larger than or equal to 0.02 ppm in presence of 3 mM Mg^{2+} are shown as grey spheres. Protons featuring at least two of these three effects are shown as cyan spheres. The positions of bound $[Co(NH_3)_6]^{3+}$ ions were defined by rMD calculations. Co^{3+} central ions are shown as large, dark blue spheres, the ammine ligands are omitted for the sake of clarity. A $[Co(NH_3)_6]^{3+}$ molecule with ligands is shown on the right for size comparison. This subfigure was prepared with MOLMOL (72), (B) and (C) Electrostatic surface representation of d3'EBS1·IBS1 displaying three patches of negative potential. The potential is represented by a color gradient from red (−667 mV) to blue (128 mV). These subfigures were prepared in PYMOL with the APBSTools2 plugin (73,74).

Figure 10. Comparison of the solution structures of the d3'EBS1·dIBS1 RNA·DNA contact and the d3'EBS1·IBS1 RNA·RNA contact. (A) Structure of d3'EBS1·IBS1 (55). (B,C) Overlay of the backbone traces of d3'EBS1·dIBS1 (light grey) and d3'EBS1·IBS1 (dark grey) (B) aligned by the backbone atoms of nucleotides 13-17 (in EBS1) and 61-65 (in dIBS1) close to the cleavage site (RMSD = 1.17 Å), and (C) aligned by the heavy atoms of the stem nucleotides (1-9 and 21-29, RMSD: 1.45 Å) showing only the G13·C65 base pair directly next to the cleavage site. (D) Electrostatic surface potential representation of d3'EBS1·dIBS1 and (E) of d3'EBS1·IBS1 depicting the strongly negative potential (indicated by the dark

color) in the tunnel formed by the major groove of the EBS1·(d)IBS1 helix. Panels (A-C) were prepared with MOLMOL (72), panels (D-E) were prepared with PYMOL with the APBSTools2 plugin (73,74), and the images of d3'EBS1·IBS1 were prepared from pdb entry 2M23.

TABLES

Table 1. Definition of the three $[Co(NH_3)_6]^{3+}$binding sites for rMD calculations of d3'EBS1·dIBS1. All protons displaying a cross peak to $[Co(NH_3)_6]^{3+}$ are sorted into three different binding sites combining protons situated close to each other in the structure calculated without metal ions.

binding site 1 d3' stem		**binding site 2 lower loop, dIBS1 5' end**		**binding site 3 dIBS1 and EBS1 5' end**	
A3	H1'	U11	H1'	G13	H1
A3	H2	U11	H6	T62	H3
G4	H1	G19	H1'	T62	CH_3(71-73)
G4	H8	G19	H8	T64	H3
U5	H3	A20	H2	T64	CH_3(71-73)
U5	H6	C59	H1'	C65	H5
A6	H1'	C59	H2''	C65	H6
U24	H1'				
U24	H6				
C26	H1'				
U27	H3				

Table 2. NMR experimental restraints and refinement statistics for the 18 lowest energy structures of d3'EBS1·dIBS1 out of 200 calculated structures.

Restraint statistics	
NOE distance restraints	733
Intraresidue	240
Interresidue	351
Long range within RNA	75
between EBS1 and dIBS1	67
total within dIBS1	161
Mean number per residue	20.4
Hydrogen bonding (base pair) restraints	82
Dihedral angle restraints	247
Mean number per residue	6.9
Residual Dipolar Coupling restraints	21
Violations	
Distance > 0.2 Å	0
Dihedral > 5°	0
RMSD (of all heavy atoms relative to the mean structure (Å))	
Global	1.00 ± 0.34
Helical stem (residues 1-9, 21-29)	0.53 ± 0.25
EBS1-dIBS1 (residues 13-19, 59-65)	0.60 ± 0.17

Table 3. Backbone torsion angles and pseudorotation angle of the EBS1 and dIBS1 residues. Values represent the average and standard deviation of five of the 18 lowest energy conformers of d3'EBS1·dIBS1 in degrees. While the backbone and ribose conformation within the EBS1 strand is typical for an A-form helix, dIBS1 is very weakly defined in its α, γ and ζ angles and β, χ and P pseudorotation angles are at intermediate values between the optima of A-form and B-form.

	G13	**G14**	**C15**	**A16**	**C17**	**U18**	**G19**	**optimum A-RNA**
α	-	−72.1 ± 0.1	−70.0 ± 1.5	−65.9 ± 2.6	−71.9± 0.3	−58.4 ± 1.0	−55.1 ± 0.9	−62
β	−172.6 ± 2.0	−171.4 ± 3.4	−188.0 ± 2.2	−188.2 ± 1.6	−187.5 ± 1.2	−177.9 ± 2.6	−187.0 ± 1.8	−180
γ	−65.0 ± 15.5	40.24 ± 1.8	57.5 ± 0.0	57.5 ± 0.0	57.6 ± 0.0	41.42 ± 1.6	41.5 ± 1.4	47
δ	84.8 ± 2.2	84.2 ± 1.6	78.1 ± 0.6	80.1 ± 0.8	80.7 ± 0.3	81.2 ± 0.4	82.2 ± 0.3	85
ε	−152.1 ± 8.2	−144.3 ± 3.5	−153.76 ± 1.8	−161.9 ± 0.0	−154.0 ± 3.3	−149.0 ± 2.2	-	−152
ζ	−83.0 ± 1.1	−68.5 ± 2.3	−63.6 ± 0.0	−83.9 ± 0.0	−63.7 ± 0.1	−63.6 ± 0.1	-	−74
χ	−147.2 ± 4.2	−145.9 ± 1.8	−167.8 ± 0.8	−164.6 ± 1.8	−161.4 ± 1.3	−156.8 ± 1.0	−158.0 ± 0.2	−160
P	10.1 ± 2.6 C3'-*endo*	0.8 ± 4.2 C2'-*exo*	19.2 ± 2.2 C3'-*endo*	27.7 ± 2.0 C3'-*endo*	8.9 ± 0.7 C3'-*endo*	15.4 ± 1.4 C3'-*endo*	22.5 ± 0.6 C3'-*endo*	18 C3'-*endo*
	C65	**T64**	**G63**	**T62**	**G61**	**A60**	**C59**	**optimum B-DNA**
α	−82.8 ± 50.0	−41.9 ± 92.7	−30.7 ± 97.5	13.7 ± 104.6	14.0 ± 108.9	−47. ± 57.3	-	−60
β	−143.2 ± 4.8	−163.6 ± 14.0	−167.3 ± 23.5	−167.9 ± 15.0	−183.6 ± 24.7	−180.3 ± 9.0	-	−180
γ	63.6 ± 57.8	90.0 ± 55.3	89.9 ± 53.5	13.4 ± 146.0	104.9 ± 14.6	24.5 ± 107.3	10.5 ± 5.0	36
δ	90.6 ± 0.9	91.2 ± 2.5	101. ± 4.5	101.6 ± 2.3	102.2 ± 16.3	117.2 ± 4.2	93.6 ± 2.0	160
ε	-	142.6 ± 44.4	133.5 ± 51.6	127.8 ± 47.4	164.2 ± 50.8	112.1 ± 53.9	182.5 ± 57.1	155
ζ	-	−21.0 ± 73.4	−0.4 ± 63.7	−7.9 ± 66.7	−42.8 ± 55.6	13.7 ± 73.0	−35.8 ± 60.6	−90
χ	−120.5 ± 1.1	−127.4 ± 1.6	−145.4 ± 2.1	−150.8 ± 5.2	−148.0 ± 3.9	−150.4 ± 2.6	−159.8 ± 0.7	−120
P	28.0 ± 1.5 C3'-*endo*	63.9 ± 6.2 C4'-*exo*	86.2 ± 13.0 O4'-*endo*	91.9 ± 3.1 O4'-*endo*	80.9 ± 37.0 C4'-*exo*	116.1 ± 9.1 C1-'*exo*	355.3 ± 2.8 C2'-*exo*	162 C2'-*endo*

Table 4. Influence of Mg^{2+}-addition on the kinetics of (d)IBS1 binding to d3'EBS1 and (d)IBS1wt binding to d3'EBS1wt as determined by SPR experiments. Listed are the arithmetic means and one standard deviation of k_{on}, k_{off} and K_D from measurements on two different sensor chips.

c(Mg^{2+}) [mM]	**k_{on} [$\mu M^{-1} s^{-1}$]**	**k_{off} [s^{-1}]**	**K_D [µM]**
dIBS1, DNA, 15 °C			
0	0.11 ± 0.04	0.18 ± 0.08	1.65 ± 0.20
1[a]	0.08	0.03	0.36
2	0.15 ± 0.07	0.02 ± 0.01	0.20 ± 0.03
5	0.19 ± 0.06	0.01 ± 0.01	0.10 ± 0.01
10[a]	0.20	0.01	0.07
20	0.19 ± 0.01	0.01 ± 0.01	0.05 ± 0.01
0[b]	0.12 ± 0.01	0.21 ± 0.04	1.60 ± 0.14
dIBS1, DNA, 25 °C			
0[c]	0.05 ± 0.02	1.45 ± 0.35	29.0 ± 5.65
1[a]	0.21	0.64	3.00
5[a]	0.24	0.18	0.72
IBS1, RNA, 25 °C			
0	0.10 ± 0.02	0.015 ± 0.010	0.15 ± 0.03
1	0.17 ± 0.08	0.006 ± 0.001	0.04 ± 0.02
5	0.21 ± 0.13	0.005 ± 0.001	0.03 ± 0.01
dIBS1wt, DNA, 15 °C			
0[ad]	-	-	747
5[ac]	0.04	0.89	25.5
20[a]	0.05	0.42	8.17
IBS1wt, RNA, 15 °C			
0[ac]	0.05	1.15	21.3
5[a]	0.05	0.14	2.92
20[a]	0.08	0.06	0.71

[a] only one measurement was performed

[b] The experiment in 0 mM Mg^{2+} was repeated (bottom row) after the one containing the highest concentration of Mg^{2+} to rule out distortion of the k_{on}, k_{off} and K_D values due to Mg^{2+}-induced degradation.

[c] rate constants are at the instrument limit

[d] rate constants are outside of the instrument limit, the affinity was determined using a fit to the equilibrium (maximal) RU values

FIGURES

Figure 1

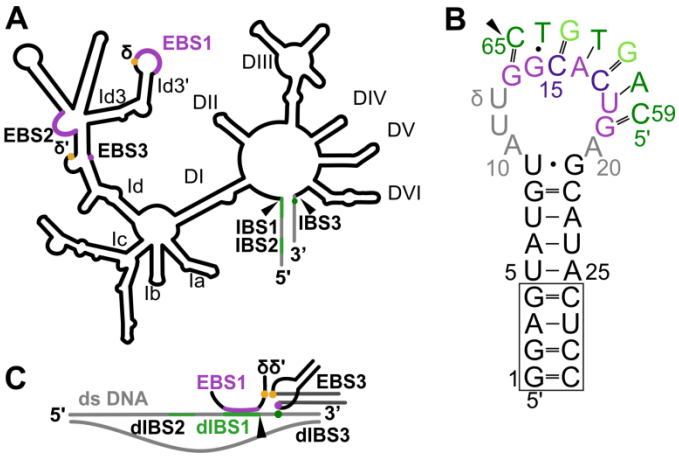

Figure 2

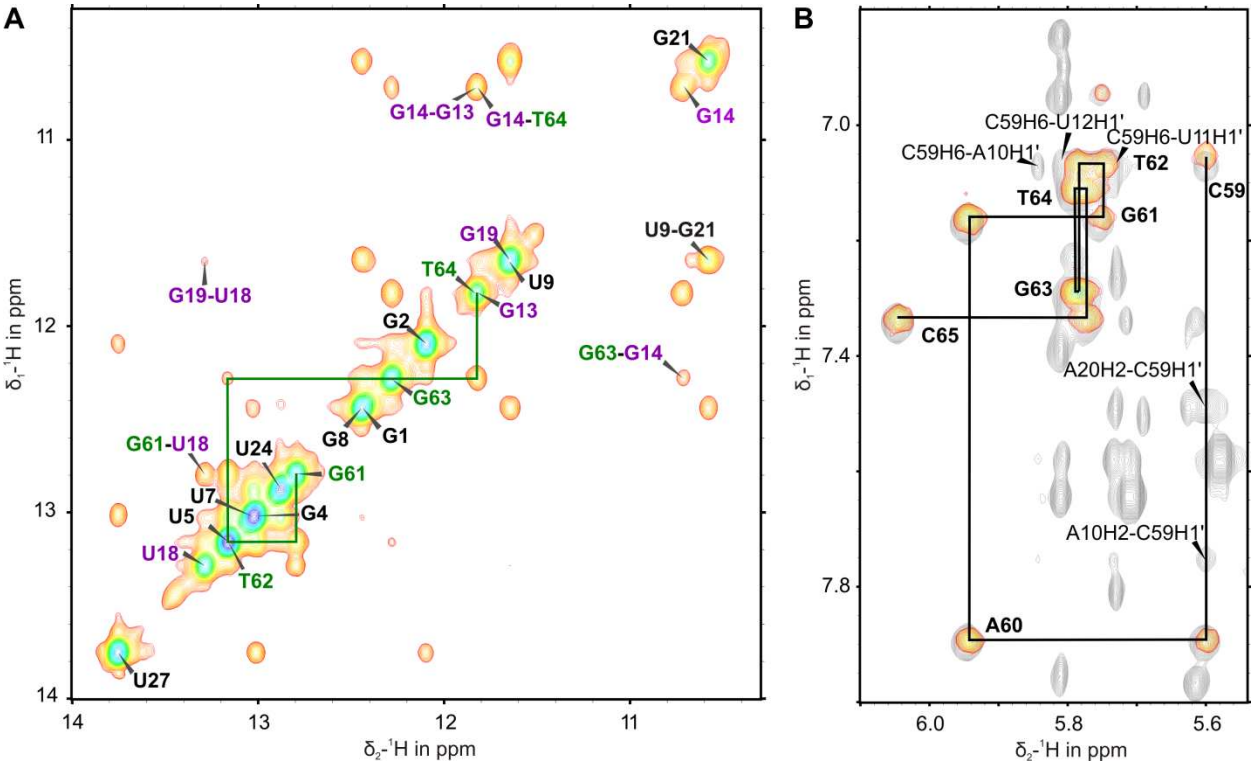

Figure 3

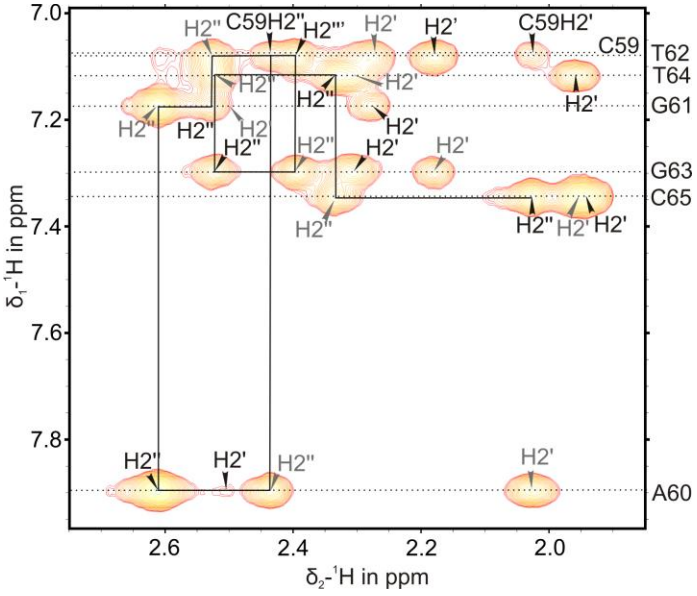

Figure 4

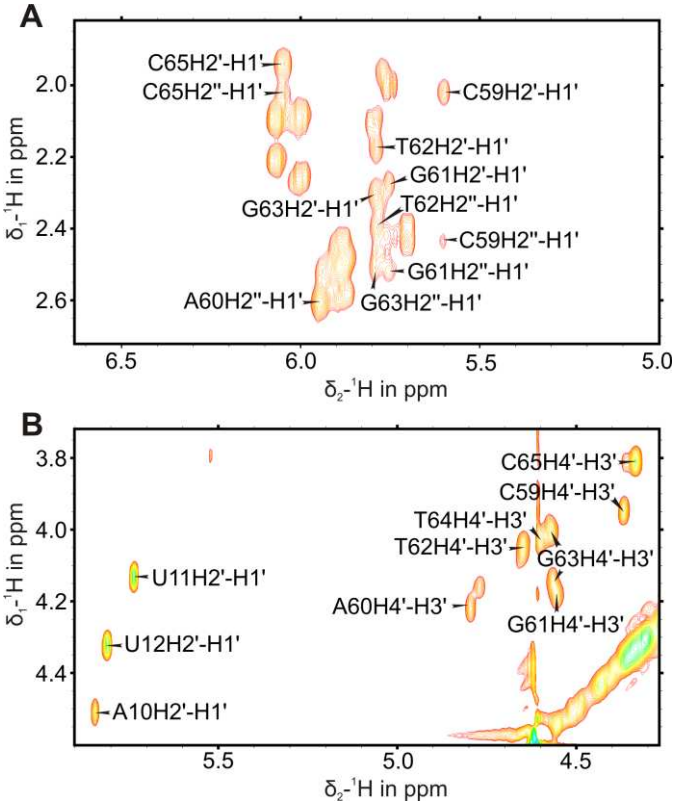

Figure 5

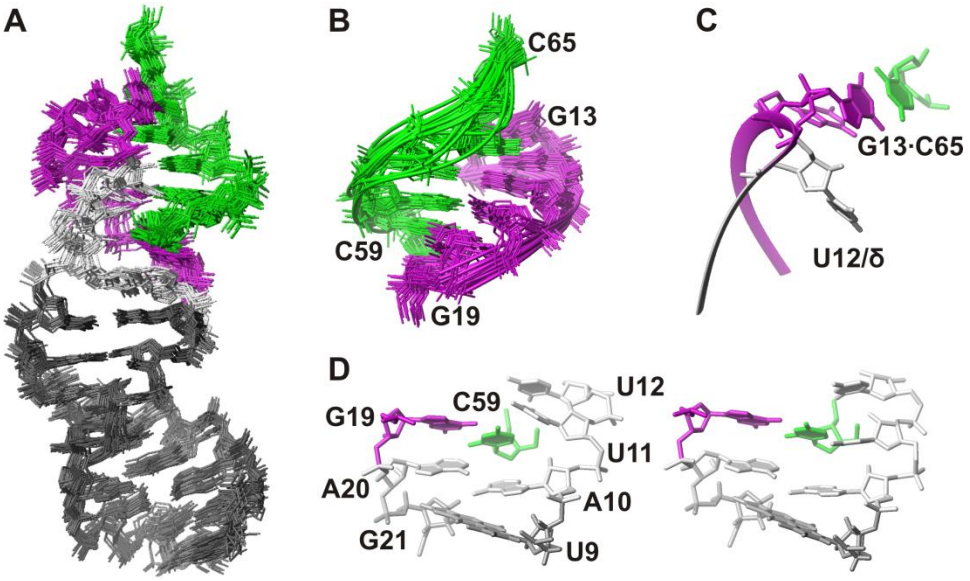

Figure 6

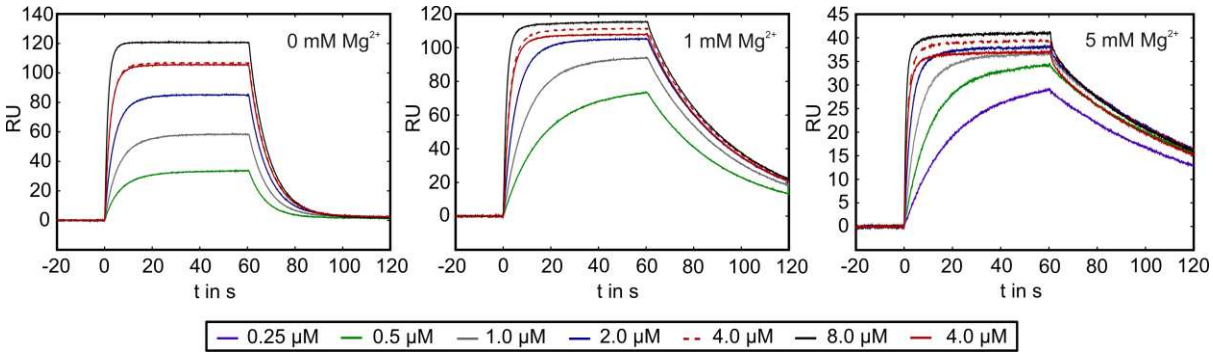

Figure 7

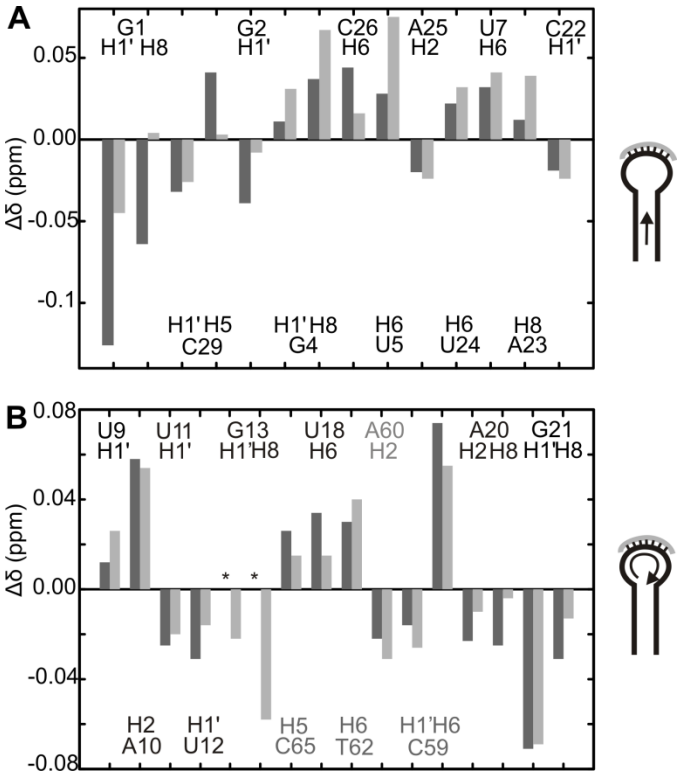

Figure 8

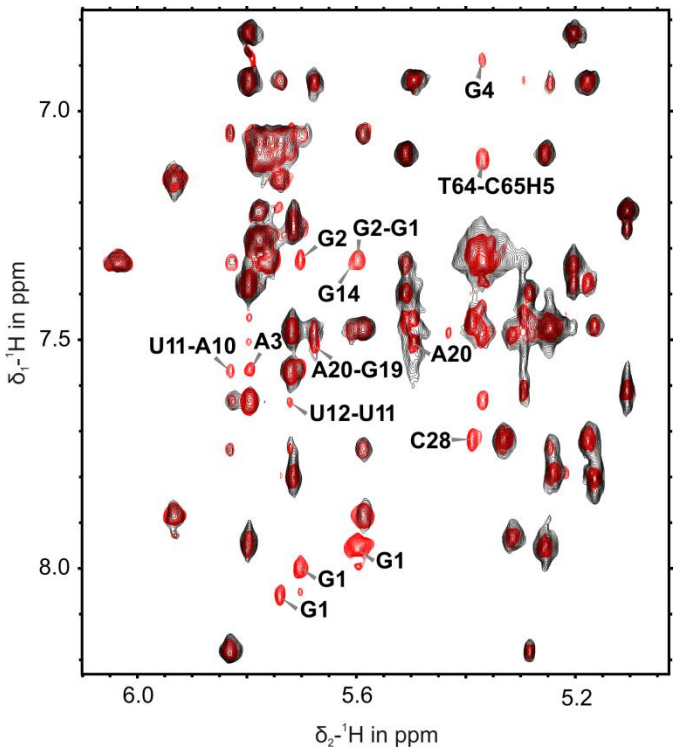

Figure 9

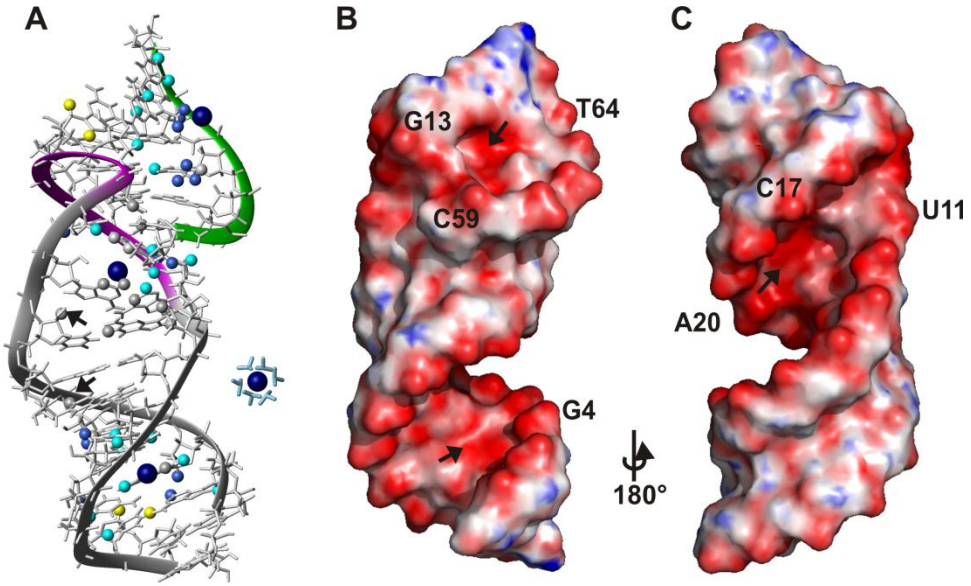

Figure 10

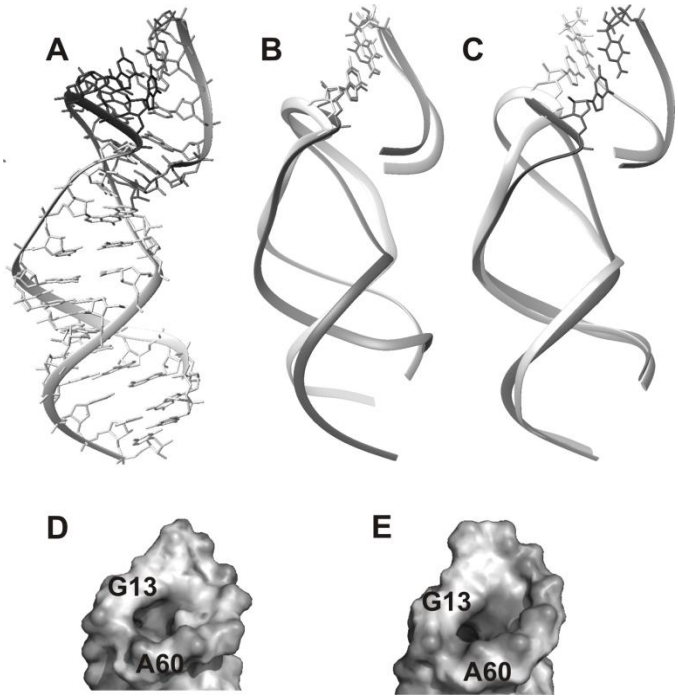

RNA:

The Role of Magnesium(II) for DNA Cleavage Site Recognition in Group II Intron Ribozymes -- Solution Structure and Metal Ion Binding Sites of the RNA·DNA Complex

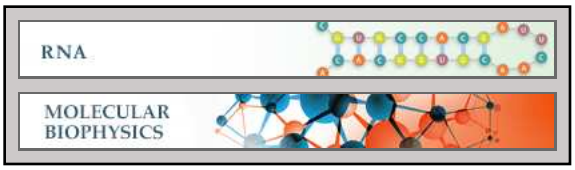

Miriam Skilandat and Roland K. O. Sigel
J. Biol. Chem. published online June 3, 2014
